JOURNAL OF PETROLOGY | VOLUME 55 | NUMBER 2 | PAGES 315–344 | 2014 | doi:10.1093/petrology/egt069

Conduit- to Localized-scale Degassing during Plinian Eruptions: Insights from Major Element and Volatile (Cl and H_2O) Analyses within Vesuvius AD 79 Pumice

THOMAS SHEA[1]*, ERIC HELLEBRAND[1], LUCIA GURIOLI[2] AND HUGH TUFFEN[3]

[1]DEPARTMENT OF GEOLOGY AND GEOPHYSICS, SOEST, UNIVERSITY OF HAWAII, HONOLULU, HI 96822, USA
[2]LABORATOIRE MAGMAS ET VOLCANS, UNIVERSITÉ BLAISE-PASCAL, CLERMONT-FERRAND, FRANCE
[3]LANCASTER ENVIRONMENT CENTRE, LANCASTER UNIVERSITY, LANCASTER, LANCASHIRE LA1 4YQ, UK

RECEIVED SEPTEMBER 11, 2012; ACCEPTED OCTOBER 25, 2013

Textural investigations of the AD 79 Vesuvius pumice emphasize the complexity of magma degassing and crystallization during the eruption, which emitted two types of pumice (white and gray) associated with different magma bodies of phonolitic and tephriphonolitic compositions respectively. These studies proposed that velocity gradients caused spatial variations in degassing within the ascending magma column at both the conduit and the localized scale. To validate this hypothesis, analyses of volatiles (Cl, H_2O) and major elements in pumice glasses and melt inclusions were performed using high spatial resolution tools (microRaman spectrometry and electron microprobe) and combined with major element and volatile concentration profiles and maps. The results indicate that the melt phase differentiated through degassing-induced crystallization of leucite, and that the gray pumice magma was efficiently homogenized prior to degassing. Because Cl diffuses more slowly than H_2O during fast ascent, it behaves as an incompatible element and can be used as a tracer of crystallization and H_2O degassing. We emphasize the importance of strain localization in generating zones of preferential exsolution and permeable pathways for gases, and establish degassing scenarios that incorporate the effects of shear-zones.

KEY WORDS: *magma degassing; crystallization; Vesuvius AD 79 pumice; volatiles in glass; chlorine; shear-zones*

INTRODUCTION

Overview

The exsolution of volatile components to a separate vapor phase can drive highly explosive eruptions; therefore, understanding the dynamics of magma degassing is of fundamental importance within the field of physical volcanology (Sparks *et al.*, 1994). When present as dissolved species within the melt, volatiles modulate phase equilibria and thus exert a direct control on magma viscosity, composition and crystallinity (Mysen & Richet, 2005). The most abundant volatiles (usually H_2O, CO_2, S, Cl, and F) have different solubilities and diffusivities within the melt, thereby regulating exsolution behavior during magma ascent and decompression (e.g. Watson, 1994; Lowenstern, 2000; Baker & Balcone-Boissard, 2009; Lesne *et al.*, 2011). The capacity to quantify volatile concentrations in magmas therefore has the potential to unravel the subtleties of magma degassing, provided that the degassing history can be recorded within the products of volcanic eruptions. Especially in the case of past eruptions for which no gas monitoring is available, quenched volcanic glasses (as pyroclast matrices or within mineral inclusions) provide some of the most useful testimonies of magma degassing because they preserve volatiles that have not

*Corresponding author. E-mail: tshea@hawaii.edu

been exsolved (Blundy & Cashman, 2008). Investigations of volatiles in highly vesicular pyroclasts and small melt inclusions are nevertheless challenging because they often require analyzing light elements such as C, H or O, in sample areas often too small to be effectively resolved by mainstream tools (e.g. Ihinger *et al.*, 1994). To overcome this problem, recent studies have emphasized the potential of microRaman spectrometry as a technique to quantify H_2O (e.g. Thomas, 2000; Di Muro *et al.*, 2006; Mercier *et al.*, 2010; Le Losq *et al.*, 2012; Shea *et al.*, 2012), and potentially CO_2 (Amalberti *et al.*, 2011; Morizet *et al.*, 2013). Sulphur and halogen species (S, Cl, F) can be accurately measured down to a few hundred parts per million by electron microprobe analysis (EMPA) (Ihinger *et al.*, 1994). In this study, we present a set of H_2O and Cl analyses performed at high spatial resolution within pumice glasses and melt or glassy inclusions (MI) from a well-studied eruption (Vesuvius AD 79). We demonstrate how such techniques allow deciphering of the large- to fine-scale intricacies of magma degassing. Some of the important questions that we aim to address through this contribution include: How do Cl and H_2O behave during magma ascent in the context of Plinian eruptions? Why do pumice clasts of similar bulk composition display textural (i.e. vesicles and crystal characteristics) and chemical (glass major element and volatile concentrations) variations within single eruptive units? Why do single pumice clasts exhibit microscale textural heterogeneities, and are those also associated with chemical variations? What is the role of magma deformation in generating such heterogeneities?

Quantification of volatiles in magma: the spatial resolution divide

The numerous techniques that have been developed to measure volatiles in volcanic glasses can be split into three main branches (see Ihinger *et al.*, 1994): (1) bulk extraction–loss-on-ignition methods [e.g. Karl-Fischer titration (KFT), thermogravimetric analysis (TGA), manometry, mainly for H_2O, CO_2 and SO_2]; (2) electron or ion beam techniques [e.g. EMPA for Cl, S, F and Br, and secondary ionization mass spectrometry (SIMS) for H_2O and CO_2]; (3) vibrational spectroscopy [Fourier-transform infrared (FTIR) and Raman], capable of measuring H_2O and CO_2. Although bulk extraction–manometry yield highly precise data (~2–5% relative), the technique is destructive and time-consuming, and cannot be used to characterize highly heterogeneous samples. EMPA is a relatively economical tool to acquire precise (~1–5% relative) measurements at high spatial resolution (~1 μm), but allows measurement of only the heavier volatiles such as Cl, F, or S [H_2O in glasses can only be estimated indirectly via the 'by-difference' method of Devine *et al.* (1995)]. SIMS offers the possibility to measure most volatiles with a high precision (<5%) (e.g. Hauri *et al.*, 2002), but has a more restricted spatial resolution (≥20 μm) and the cost per analysis is high. Conversely, FTIR and microRaman spectroscopies are cheap, and allow for a high number of analyses per hour without damaging the sample (Thomas, 2000; Mercier *et al.*, 2010). Despite the need for extensive sample preparation (double-polishing), FTIR typically yields precise measurements (~10% relative); however, the instrument is usually incapable of resolving areas smaller than 10–30 μm, which is too large for thin pyroclast glass walls or small glassy inclusions. In comparison, confocal microRaman spectroscopy allows very high spatial resolutions (~1–2 μm) and good precision (~5–15% relative) but requires more calibration standards (Di Muro *et al.*, 2006). Recently, Mercier *et al.* (2010), Métrich *et al.* (2010) and Shea *et al.* (2012) presented some of the first applications of this method to measure water within MI and groundmass glasses in natural samples.

H_2O and Cl in magmas: contrasting behaviors

Volatiles in magmas start to exsolve at various depths, exsolution conditions depending on solubility, concentration within the melt (i.e. whether initially saturated or undersaturated), the coexistence with other volatile species (e.g. $H_2O + CO_2$) and the rates of ascent (Rutherford, 2008). Because different species diffuse at different rates, given a fixed temperature and composition (Watson, 1994), each species records different fractions of the storage, ascent and eruption history. Hence, whenever possible, measurements of H_2O are complemented with analyses of other volatiles; for example, when CO_2 is detectable, determining its contribution to the dissolved volatile budget aids greatly in reconstructing the magma ascent path and degassing style (e.g. equilibrium vs disequilibrium, open vs closed system) (Blundy & Cashman, 2008; Métrich & Wallace, 2008). In glasses or melt inclusions in which CO_2 is absent or close to the detection limit (e.g. Cioni, 2000), other volatiles may be considered. Because S and halogens can be precisely measured using EMPA (detection limits ~30 ppm and 120 ppm with relative precisions of <5 and <10% for Cl and F respectively; Balcone-Boissard *et al.*, 2010), they can serve as potential tracers of macro- to micro-scale degassing within vesicular pyroclasts. Pumice glasses from the AD 79 Vesuvius eruption contain abundant halogens (Cl and F) but little to no S (see below). In this study we focus on the combined behavior of Cl and H_2O to examine magma degassing during this eruption.

Compared with other volatile species, the degassing of Cl is subject to additional complications: first, below certain pressures (typically <200 MPa) Cl-saturated melts can coexist with two separate fluid phases, an H_2O-rich, Cl-bearing vapor, and a Cl-rich brine (e.g. Webster, 2004; Carroll, 2005). As a result, the partitioning behavior of chlorine between the vapor phase driving explosive eruptions and the melt is more difficult to predict (Gardner *et al.*, 2006). Second, unlike H_2O or CO_2 (Fig. 1a), the

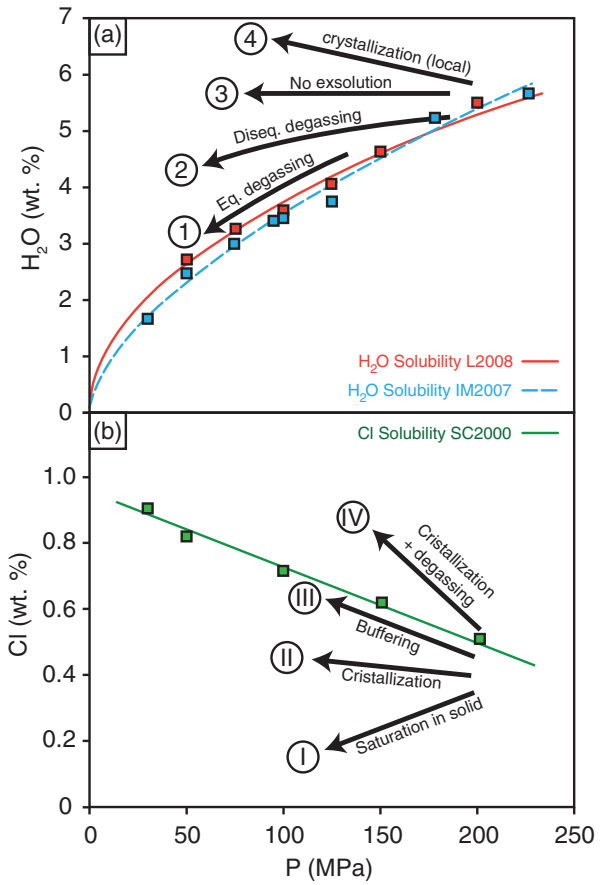

Fig. 1. Illustrations of volatile behavior of a phonolite melt initially saturated in both H_2O and Cl. (a) The decompressing melt can track an equilibrium degassing path if exsolution of the vapor phase can respond efficiently to decreasing solubility [curves of Iacono-Marziano *et al.* (2007) (IM2007) and Larsen (2008) (L2008) for phonolites] (1). If exsolution cannot keep up with decreasing solubility, the melt undergoes disequilibrium degassing (2) or, in extreme cases, water does not exsolve (3). Growth of crystals (e.g. spherulites) can also locally concentrate H_2O in the surrounding melt (4) (e.g. Gardner *et al.*, 2012). (b) The behavior of Cl is more complex; solubility increases with decreasing pressure [values from Signorelli & Carroll (2000)], and the melt may coexist with both an H_2O-rich vapor and a Cl-rich brine. Cl concentration in the melt can decrease during decompression if a Cl-bearing phase crystallizes in sufficient abundance (I). If, on the other hand, Cl is not incorporated within crystallizing phases, residual Cl concentrations increase (II) (at a smaller scale, minor increases in residual Cl could also be expected during loss of H_2O during degassing). The magma will follow Cl solubility if a coexisting Cl-rich fluid phase is present and 'buffers' or increases the Cl concentration in the melt (III). Finally, Cl degasses if a high rate of crystallization is achieved during decompression, effectively forcing the melt to stay above or cross the solubility curve (IV).

solubility of chlorine within the melt increases with decreasing pressure (e.g. Signorelli & Carroll, 2000; Carroll, 2005) (Fig. 1b). This implies that as magmas decompress, reaching the conditions for Cl supersaturation, exsolution becomes increasingly difficult (e.g. Gardner *et al.*, 2006). Such conditions can be reached if crystallization is extensive and rapid enough to cause Cl supersaturation (Fig. 1b). Any other situation will typically lead to increases of Cl in the residual melt, or Cl saturation within a mineral phase (e.g. apatite, sodalite). If the other variables linked to Cl variations in measured pyroclast glasses can be well constrained (e.g. crystallization of mineral phases, loss of H_2O), the complexities inherent in the study of Cl can be turned to our advantage to understand degassing in magmas at a much finer spatial scale.

Conduit- to micro-scale heterogeneities in tephra

The products of explosive eruptions consistently display degassing-induced textural heterogeneities (i.e. heterogeneities that are not associated with magma mixing processes) at all scales. At the large scale (i.e. the scale of an eruptive sequence to an eruptive unit), pyroclasts are known to display substantial variations in vesicularity (see Houghton & Wilson, 1989), or microlite abundances (see Blundy & Cashman, 2008). Characterizing such heterogeneities through textural investigations has now become common practice to interpret degassing history (e.g. Polacci *et al.*, 2001, 2003; Gurioli *et al.*, 2005; Adams *et al.*, 2006; Lautze & Houghton, 2007; Shea *et al.*, 2010*b*, 2012). At the clast scale (centimeter to millimeter), textural heterogeneities include shear-zones, tube-vesicles, banding or foliations, crystal-aggregates, and, at an even smaller scale (<100 μm), they can take the form of elongate vesicles or crystals with preferred orientations (e.g. Martí *et al.*, 1999; Polacci *et al.*, 2001, 2003; Rosi *et al.*, 2004; Castro *et al.*, 2005; Lautze & Houghton, 2007; Wright & Weinberg, 2009; Wright *et al.*, 2011). These types of heterogeneities frequently bear the imprint of strain localization occurring at the conduit wall margins (e.g. Stasiuk *et al.* 1996; Tuffen *et al.*, 2003) or even across the conduit (e.g. Polacci *et al.*, 2003; Wright & Weinberg, 2009; Shea *et al.*, 2012). Using numerical models, Hale & Mühlhaus (2007) found that the formation of shear-zones reduces the friction between the magma and the conduit walls, and decreases overpressure within the upper conduit. Localized shearing of viscous magmas can also result in heating by tens of degrees (Hess *et al.*, 2008). More generally, deforming vesicles provide free slip surfaces to reduce local viscosity (Llewellin *et al.*, 2002) in addition to promoting permeable outgassing (e.g. Burgisser & Gardner, 2005; Okumura *et al.*, 2009; Degruyter *et al.*, 2010; Laumonier *et al.*, 2011). The capacity to characterize the link between textural heterogeneities resulting from strain localization and volatiles within pyroclast glasses is thus essential in determining the processes that influence the behavior of magmas during slow and/or fast ascent.

Throughout this contribution, we refer to textural and chemical heterogeneities at the scale of one or several eruptive units as 'large-scale' or 'conduit-scale' (i.e. heterogeneities between different clasts assuming pyroclasts

represent the state of the magma at the fragmentation level), and at the scale of a few bubbles to the scale of a single clast as 'small-scale' or 'micro-scale'.

TEXTURAL, PETROLOGICAL AND GEOCHEMICAL CHARACTERISTICS OF THE AD 79 PUMICE

Brief summary of the eruption sequence

The eruption of Vesuvius (Italy) in AD 79 has been extensively studied in the past 40 years, and we refer to previous studies (Sigurdsson *et al.*, 1985; Cioni *et al.*, 1992, 1995, 2004; Gurioli *et al.*, 2002) for detailed descriptions of the sequence of events and deposits; only the most relevant information is given here.

The eruption started in the fall of AD 79, and expelled over 3 km^3 dense-rock equivalent (DRE; Cioni *et al.*, 1995) of pumice material in just over 30 h, causing the destruction of Roman towns and villas in the vicinity of the volcano (Fig. 2) (Sigurdsson *et al.*, 1985). Eight major eruptive units EU1–EU8 were described by Cioni *et al.* (1992), with two main phases: a 'magmatic' phase from EU1 to EU3 and a 'phreatomagmatic' phase from EU4 to EU8. Prior to the eruption, a tephritic magma intruded a previously existing phonolitic magma reservoir. These magmas mixed within a large portion of the main reservoir, forming an intermediate tephriphonolitic magma underneath a smaller volume of unmixed phonolitic magma. As a result, about 7 h into the eruption, the bulk magma composition shifted from phonolite to tephriphonolite and the pumice color changed from white (EU1–EU2) to gray (EU3 and onwards). During the first half of the eruption, the plume was dominantly stable and the material deposited was dominantly fall pumice with a few intercalated partial collapse pyroclastic density currents (PDCs) (Cioni *et al.*, 1992). The activity then changed to a dominantly unstable eruptive column regime, which saw the generation of highly destructive PDCs that effectively obliterated the towns of Pompeii and Herculaneum amongst others. In this study we focus on the products of the eruptive phase from EU2 to EU4 (10 eruptive units; see Fig. 2), which represent most of the ejected volume (Cioni *et al.*, 1995).

Petrological and geochemical characteristics of the AD 79 pumice

The petrology and geochemistry of the two erupted end-member compositions (phonolite and tephriphonolite) were characterized by Sigurdsson *et al.* (1990), Civetta *et al.* (1991), Mues-Schumacher (1994) and Cioni *et al.* (1995). The white and the gray pumice both have phonolitic groundmass glass compositions, with higher Al_2O_3 and lower TiO_2, MgO, FeO and CaO in the white pumice glasses (Mues-Schumacher, 1994; Cioni *et al.*, 1995). The main phenocryst phases occurring in both white and gray pumice consist of sanidine (~0·5–5 vol. % on a vesicle-free basis), leucite (~0·5–2 vol. %), and pyroxenes (both diopside and salite, 0·5–4 vol. %), with minor melanitic garnet, ferripargasitic amphibole and phlogopite (Cioni *et al.*, 1995). Sr isotope data show that most of the sanidine phenocrysts crystallized within the white pumice magma (Sigurdsson *et al.*, 1990; Civetta *et al.*, 1991; Morgan *et al.*, 2006). Microphenocryst and microlite assemblages generally comprise leucite, with sparser sanidine, pyroxene, amphibole, phlogopite, and sodalite (see Plate Al in the Supplementary Data; supplementary material is available for downloading at http://www.petrology.oxfordjournals.org).

Interpreting pumice textures in terms of degassing processes requires the magma to be fairly homogeneous prior to ascent and decompression. If, for instance, pyroclasts derive from mingled magmas, isolating compositional changes that stem from the initial magma chemistry from those that derive from degassing becomes problematic. In the case of the AD 79 eruption, Sigurdsson *et al.* (1990), and later Civetta *et al.* (1991) and Cioni *et al.* (1992, 1995) all suggested that the gray pumice magma was variably mingled and mixed during the course of the eruption. In contrast, Mues-Schumacher (1994) referred to a well-homogenized gray pumice magma prior to its escape from the reservoir. As we discuss below, our glass compositions, collected from a wide range of stratigraphic units, refute the hypothesis of an important effect of syn-eruptive mixing on the gray magma composition. Instead, we argue for a homogeneous gray magma prior to significant decompression, and thus for a degassing origin of the observed textures and interstitial glass compositions. Sigurdsson *et al.* (1990), Mues-Schumacher (1994) and Cioni *et al.* (1995) also noted the presence of rare mingled pumices within the unit corresponding to the transition between the white and the gray pumice magma (EU2/3pf, Fig. 2). Herein, this problem was avoided by selecting only pumice clasts lacking obvious white and gray magma mingling features.

Previous textural and volatile investigations

Pumice clasts from the Vesuvius AD 79 eruption were selected for this study for several motives. First, this eruption has been well characterized petrologically (e.g. Sigurdsson *et al.*, 1990; Cioni *et al.*, 1995), and has already been the subject of several textural investigations (Gurioli *et al.*, 2005; Shea *et al.*, 2009, 2010*a*, 2011, 2012). Second, the pumice glasses from this eruption are known to contain at least three volatiles in high abundance (H_2O, Cl and F) that can be used to test the combination of Raman analysis and EMPA. Third, a number of studies have already examined the behavior of volatiles in both pumice glasses and glassy inclusions (Cioni, 2000; Balcone-Boissard *et al.*,

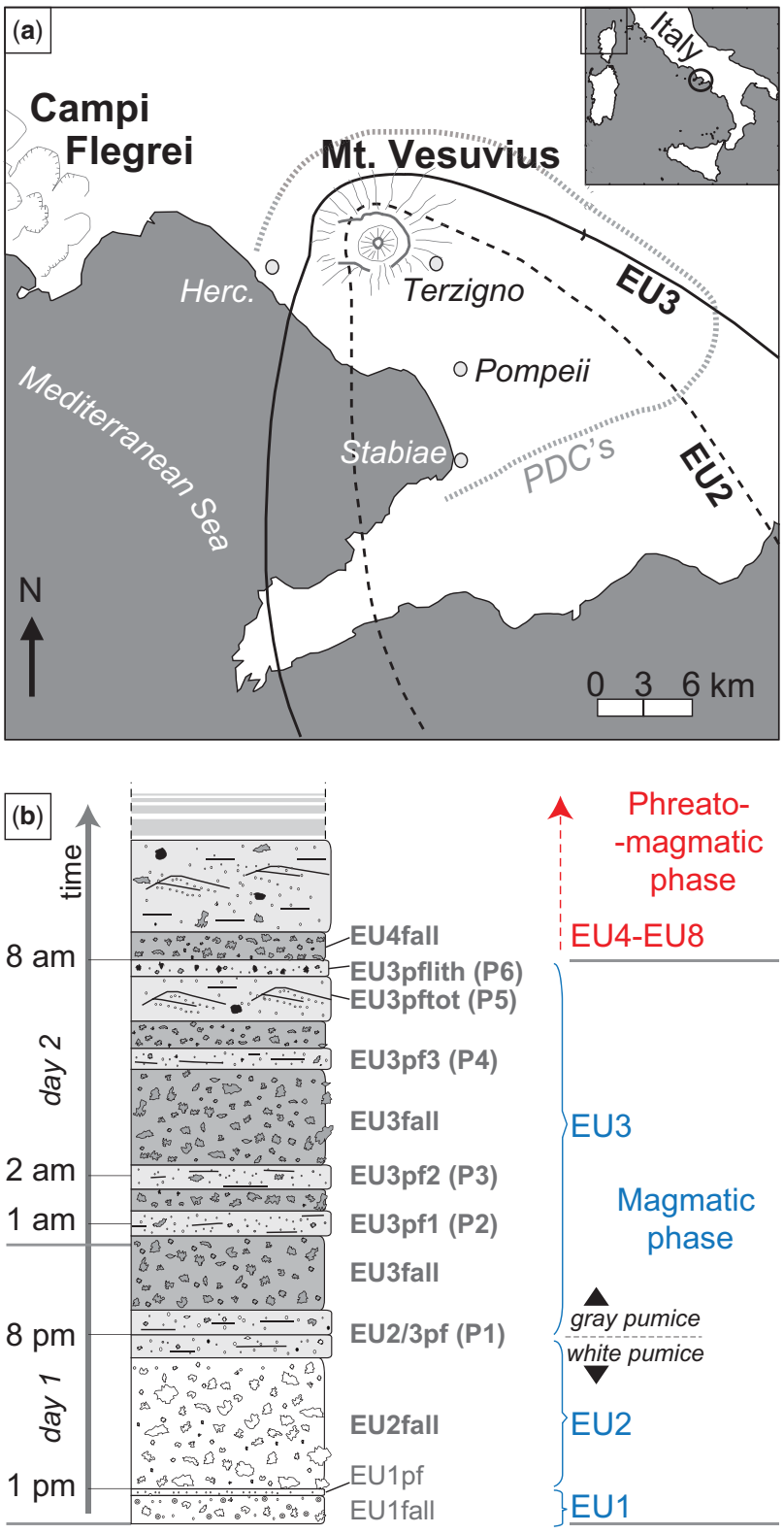

Fig. 2. (a) Location map of Mt. Vesuvius showing the 10 cm isopachs of fall deposits for EU2 and EU3 (continuous and dashed black lines), and the distribution of pyroclastic density current deposits (PDCs, dotted gray line). (b) Stratigraphy of the magmatic (EU1–EU3) and the start of the phreatomagmatic (EU4 onwards) phases of the AD 79 eruption of Vesuvius using an eruptive unit nomenclature ('EU') adopted from Cioni *et al.* (2004) and the simplified PDC nomenclature ('P') of Shea *et al.* (2011). Figure modified from Shea *et al.* (2012), with isopachs from Cioni *et al.* (1992, 2004).

2008, 2011; Shea *et al.*, 2012), providing us with helpful information to set up our high spatial resolution study.

Because this contribution explores the link between pyroclast textures and their volatile contents, we first provide a brief summary of the most significant outcomes from recent textural studies focusing on AD 79 pumice, as well as investigations of volatiles in groundmass glasses and melt inclusions.

Textural investigations

Gurioli *et al.* (2005) and later Shea *et al.* (2010*a*, 2011, 2012) characterized the textures of pumices from both the main fall units of the eruption (EU1, EU2, EU3base, EU3max, EU3top, and EU4) and the main pyroclastic density current units [EU2/3pf, EU3pf1, EU3pf2, EU3pf3, EU3pftot, and EU3pfLith; renamed P1–P6 for simplicity by Shea *et al.* (2011)] (Fig. 2). It was found that pumice textures contained evidence for continuous nucleation of bubbles, nonlinear ascent and decompression styles (slow initial ascent and rapid acceleration towards the upper conduit), and extensive 'maturation' of bubbles prior to fragmentation (bubble coalescence and collapse). Shea *et al.* (2009) also found that leucite microphenocrysts probably crystallized during the initial stages of slow decompression rather than during fast ascent. Notable differences were observed between pumice clasts from the white and gray magmas; white pumice clasts typically preserve textures reminiscent of the earlier stages of degassing compared with the gray pumice. Even though the white magma ascended more slowly than the gray magma (Shea *et al.*, 2011, 2012), the kinetics of degassing were slower owing to the lower temperatures (~830–925°C and ~1000–1050°C for white and gray magmas respectively). It was also noted that most pumices contained clear evidence of strain localization (shear-zones, dense bands, and deformation gradients at the clast-scale) (see Plate A2 in the Supplementary Data). These textures were interpreted to reflect lateral velocity gradients within the conduit, with faster-ascending magma being concentrated at the core of the conduit and slower-ascending magma being found toward the margins. Based on the pyroclast textures observed, a preliminary model of the birth and evolution of localized deformation zones in magmas was proposed by Shea *et al.* (2012), whereby early shear-zones take the form of sets of vesicles elongated in the direction of shear, and progressively transform into dense bands as these vesicles coalesce and collapse during outgassing. One of the objectives of the present study is to provide geochemical constraints (major element and volatile analyses) that can help better constrain and identify the various stages of strain localization.

Previous volatile studies: Cl

Cioni *et al.* (1995), Signorelli & Capaccioni (1999) and Cioni (2000) reported high Cl in matrix glasses and melt inclusions (~0·4–0·8 wt %), and suggested that the white magma, as well as a portion of the gray magma, was initially saturated with both a Cl-rich immiscible brine and a Cl-bearing, H_2O-rich vapor. The lack of Cl variations within MI suggest that the presence of such sub-critical fluids provided a Cl 'buffer' for the melt at depth. In addition, they interpreted the lack of strong changes in Cl within most pumice glasses to reflect little to no syn-eruptive chlorine exsolution. Recently, their findings were corroborated by additional measurements of Cl performed by Balcone-Boissard *et al.* (2008, 2011).

Previous volatile studies: H_2O

Cioni (2000) analyzed water and other volatiles within MI in both the white and gray pumice and found that the white phonolitic magma initially contained about 6 wt % H_2O, and that the mafic end-member that initially intruded the salic reservoir contained ~3–3·5 wt % H_2O. The gray magma was efficiently mixed before ascent and degassing, which rules out the development through time of a strong vertical volatile gradient. Cioni (2000), on the basis of the inferred geometry of the reservoir, suggested that the white magma also had a fairly homogeneous H_2O content. In keeping with these studies, we make the assumption that no significant volatile gradients were present within the white and gray magma bodies prior to the eruption. Balcone-Boissard *et al.* (2011) determined whole-rock water contents between 0·5 and 2·4 wt % water (values corrected for phenocryst contents), and deduced from corresponding pumice textures that the white magma underwent closed-system degassing. Shea *et al.* (2012) measured 0–2·3 wt % water within the glassy mesostasis of the gray pumice and concluded that the gray magma experienced disequilibrium degassing followed by the development of permeability and outgassing.

Previous volatile studies: CO_2, S, and F

No magmatic CO_2 or S was detected by Cioni (2000) within MI representing the phonolitic compositional end-member, which is rather surprising considering the abundance of carbonate rock formations under Vesuvius. In contrast, he measured both volatiles (CO_2 ~1500 ppm, S ~1400 ppm) within melt inclusions representing the mafic magma feeding the existing reservoir prior to the eruption, suggesting that a substantial amount of carbon dioxide and sulphur was degassed at the relatively shallow storage depths (estimates for the shallow reservoir vary between 4 and 8 km depending on the inferred participation of CO_2 in phase assemblages; Cioni, 2000; Scaillet *et al.*, 2008; Shea *et al.*, 2009). Although CO_2 is not reported for AD 79 pumices, carbonates ($CaCO_3$) are often found as micro- to macroscopic inclusions within the groundmass glass; this has some importance for any bulk volatile analyses, as any dissolved or heated carbonate can potentially contribute to a non-magmatic CO_2 signature.

F is abundant within the AD 79 pumice glasses and glassy melt inclusions (~2000–8000 ppm) and behaves mostly in an incompatible fashion during degassing, increasing slightly within the residual melt (e.g. Cioni, 2000; Balcone-Boissard *et al.*, 2008).

The potential influence of 'secondary' hydration

Volcanic glasses exposed to atmospheric conditions for prolonged periods of time can incorporate meteoric water into their structure (Friedman & Smith, 1958). This water enters the framework in molecular form (H_2O_m) or as hydroxyls (OH) depending on the temperature and total water content (Roulia *et al.*, 2006), and, given sufficient time (thousands to hundreds of thousands of years), can diffuse across tens to hundreds of microns into the aluminosilicate (e.g. Anovitz *et al.*, 2008; Yokohama *et al.*, 2008; Giachetti & Gonnermann, 2013). This type of water is referred to here as 'secondary' water (i.e. as opposed to 'primary' magmatic water). Even though the AD 79 pumice clasts are only ~2000 years old, the possible influence of secondary water has never been thoroughly assessed. Recent studies by Roulia *et al.* (2006) and Denton *et al.*, (2009, 2012) have shown that thermogravimetric analysis (TGA) can be used to distinguish 'primary' from 'secondary' water. Before robust intepretations can be made regarding the degassing of primary volatiles during the AD 79 eruption, we thus need to assess any potential contribution of secondary water.

METHODS

H_2O concentration was quantified using microRaman spectroscopy and Cl by EMPA. For these volatiles, point analyses as well as one detailed chemical profile were obtained. Four semi-quantitative high spatial resolution element maps of Cl were also acquired by microprobe. In addition, to investigate the possibility that secondary meteoric hydration occurred within pumice glasses during the past 2000 years, volatile release heating curves were obtained using TGA.

Choice of pumice glasses and glassy inclusions

As in the study by Shea *et al.* (2012), three thin sections of AD 79 pumice were made for each eruptive unit (11 eruptive units in total), representing the low-, modal- and high-density (or high-, modal- and low-vesicularity respectively) end-members of a 100-clast distribution (Table 1). Only one of the two initial white pumice units was analyzed (EU2), whereas all nine units from the gray pumice of the magmatic phase of the eruption (EU3) and one unit from the phreatomagmatic phase (EU4 fall) were measured. Owing to the high vesicularity of most pumice clasts, finding glass areas large enough to measure was often problematic. As a result, particular attention was given to analyzing glass nodes (i.e. the glass areas between three or more bubbles) ≥8–10 μm in diameter to ensure that only the center of the area was measured. Textural heterogeneities within a single thin section (e.g. a lighter more vesicle-rich zone and a darker denser zone) were prevalent enough to warrant two separate sets of analyses. This allowed us to test whether these textural heterogeneities also translated into chemical variations. Hence, for each clast, two separate measurements are given (Tables 1 and 2).

Numerous melt inclusions were exposed on the surface of the thin sections used to analyze matrix glasses. These were almost exclusively enclosed within salite (a high-Fe clinopyroxene) and diopside. As noted by Cioni (2000), those minerals predominantly formed within the white magma before being mixed into the tephrite; thus, it is expected that these inclusions will serve to trace the composition of only the white magma prior to eruption. A few melt inclusions hosted in sanidine or leucite were also analyzed but typically contained low water contents and often displayed pervasive fracturing. Consequently, only pyroxene-hosted inclusions were chosen for detailed Raman analysis and EMPA (Table 3). Because inclusions were measured directly on polished thin sections, they did not undergo any homogenization step. No correction for potential post-entrapment crystallization, re-equilibration with outside melt or H_2O loss by diffusion were performed, as those types of procedures are not well calibrated or routinely performed for minerals other than olivine or pyroxenes in mafic melts (see Kent, 2008; Métrich & Wallace, 2008). Compared with more robust melt inclusions studies performed using heating stages (e.g. Cioni, 2000), the obvious disadvantage to this analytical strategy is that there is a fair amount of uncertainty as to how accurately the inclusions represent the parent melt compositions. On the other hand, acquisition of data for numerous melt inclusions is fairly rapid, with the advantage that the host clast is fully characterized texturally and chemically.

Quantification of H_2O using Raman spectrometry

Raman scattering (i.e. a form of inelastic photon interaction) occurs when a monochromatic laser illuminates a glassy sample. This scattering depends on the composition and molecular structure of the aluminosilicate framework, as well as the abundance of hydrogen- and carbon-bearing molecules (McMillan, 1984; Mercier *et al.*, 2009; Morizet *et al.*, 2013). The Raman spectrum of a hydrous glass typically contains two regions of interest (e.g. Thomas, 2000; Zajacz *et al.*, 2005; Behrens *et al.*, 2006; Di Muro *et al.*, 2006) (Fig. 3a): (1) a region composed of three main peaks between ~200 and 1200 cm^{-1}, attributed to vibrations produced by the aluminosilicate framework (tetrahedrally coordinated cations, chiefly Si^{4+}, Al^{3+}, Fe^{3+}, bonded to

Table 1: Textural and volatile data for AD 79 pumice glasses

Eruptive unit	Sample[1]	ISH[2]	ρ[3]	φ (%)[4]	Cl (wt %)	H_2O (wt %)[5]	dP/dt[6]	Modeled Lc (vol. %)[7]	Measured Lc (vol. %)[7]
EU2	15-2-11__1	1·3	low	83·4	0·688 (0·031)	0·76 (0·35)*	0·98	15·52	13·00
	15-2-11__2				0·696 (0·025)			12·77	
	15-2-3__1		modal	77·0	0·658 (0·045)	0·46 (0·20)*	1·13	11·51	14·00
	15-2-3__2				0·655 (0·022)			9·88	
	15-2-5__1		high	70·9	0·635 (0·014)	0·54 (0·07)*	1·15	5·92	17·50
	15-2-5__2				0·672 (0·033)			10·54	
P1	26-1-5__1	1·8	low	77·9	0·691 (0·023)	1·73 (0·25)*	3·19	17·15	28·38
	26-1-5__2				0·690 (0·033)			18·03	
	26-1-7__1		modal	70·8	0·636 (0·022)	1·89 (0·26)*	3·77	9·04	15·86
	26-1-7__2				0·627 (0·018)	1·43 (0·25)		8·09	
	26-1-11__1		high	67·9	0·681 (0·021)	1·57 (0·14)*	5·01	16·36	21·10
	26-1-11__2				0·715 (0·024)			21·13	
EU3base	12-8-29__1	2·1	low	76·9	0·650 (0·025)	1·04 (0·17)*	7·78	12·57	28·66
	12-8-29__2				0·672 (0·027)	0·67(0·14)		13·84	
	12-8-13__1		modal	64·5	0·709 (0·009)	0·18 (0·16)*	3·17	20·50	21·18
	12-8-13__2				0·692 (0·044)	018 (0·16)		19·39	
	12-8-37__1		high	50·1	0·707 (0·023)	0·00 (0·15)*	2·35	22·66	19·30
	12-8-37__3				0·747 (0·031)	0·00 (0·15)		23·01	
EU3max	12-9-42__1	2·7	low	67·4	0·634 (0·019)	1·4 (0·30)*	6·63	7·82	17·70
	12-9-42__2				0·716 (0·039)	0·85 (0·10)		17·41	
	12-9-16__1		modal	59·6	0·655 (0·014)	0·74 (0·25)*	6·20	17·14	20·77
	12-9-16__2				0·685 (0·017)	0·85 (0·07)		20·14	
	12-9-37__1		high	52·2	0·740 (0·021)	0·24 (0·23)*	4·65	23·87	35·15
	12-9-37__2				0·814 (0·048)			25·20	
P2	27-1-9__1	2·9	low	83·7	0·668 (0·020)	1·20 (0·07)*	10·95	15·31	17·55
	27-1-9__2				0·686 (0·002)			15·77	
	27-1-30__1		modal	66·2	0·657 (0·005)	1·18 (0·14)*	4·38	11·65	17·81
	27-1-30__2				0·687 (0·029)			14·69	
	27-1-4__1		high	52·6	0·778 (0·027)	1·06 (0·19)*	5·70	22·74	32·83
	27-1-4__2				0·879 (0·025)			23·67	
P3	28-1-32__1	3·3	low	74·1	0·655 (0·026)	1·46 (0·07)*	8·45	11·09	18·36
	28-1-32__2				0·653 (0·022)	0·65 (0·27)		10·01	
	28-1-12__1		modal	67·6	0·674 (0·035)	0·45 (0·11)*	6·59	12·69	16·15
	28-1-12__2				0·670 (0·021)			13·05	
	28-1-1__1		high	52·8	0·702 (0·030)	0·33 (0·16)*	5·54	19·77	34·78
	28-1-1__2				0·738 (0·022)			20·46	
P4	19-1-21__1	3·7	low	74·0	0·706 (0·014)	1·07 (0·14)*	9·55	14·12	24·16
	19-1-21__2				0·757 (0·045)	0·89 (0·19)		17·65	
	19-1-4__1		modal	67·9	0·680 (0·024)	0·82 (0·29)*	8·08	16·50	32·31
	19-1-4__2				0·736 (0·040)	0·40 (0·14)		18·04	
	19-1-10__1		high	51·9	0·631 (0·014)	0·38 (0·11)	7·72	12·81	24·96
	19-1-10__2				0·655 (0·013)	0·14 (0·02)*		14·72	

(continued)

Table 1: Continued

Eruptive unit	Sample[1]	ISH[2]	ρ[3]	φ (%)[4]	Cl (wt %)	H_2O (wt %)[5]	dP/dt[6]	Modeled Lc (vol. %)[7]	Measured Lc (vol. %)[7]
EU3top	20-1-31__1	3·9	low	80·0	0·642 (0·034)	1·19 (0·23)*	11·53	7·90	22·25
	20-1-31__2				0·637 (0·009)	1·01 (0·03)		9·76	
	20-1-4__1		modal	72·0	0·688 (0·029)	1·03 (0·21)*	11·07	15·63	34·64
	20-1-4__2				0·706 (0·054)			13·82	
	20-1-5__1		high	55·7	0·661 (0·025)	0·80 (0·13)	5·83	13·44	35·85
	20-1-5__2				0·689 (0·027)	0·24 (0·04)*		20·28	
P5	21-1-52__1	4·3	low	82·4	0·688 (0·022)	1·57 (0·08)*	12·75	15·15	35·57
	21-1-52__2				0·688 (0·056)	1·20 (0·06)		16·59	
	21-1-10__1		modal	73·4	0·699 (0·033)	1·49 (0·16)*	8·55	13·56	22·63
	21-1-10__2				0·668 (0·023)	1·19 (0·04)		10·94	
	21-1-2__1		high	58·1	0·648 (0·042)	1·15 (0·18)*	4·46	18·18	22·90
	21-1-2__2				0·656 (0·024)			14·89	
P6	22-4-8__1	4·6	low	77·5	0·706 (0·034)	2·10 (0·34)	0·25	12·69	23·38
	22-4-35__1		modal	62·1	0·806 (0·019)	1·88 (0·21)	0·16	20·71	27·18
	22-4-35__2				0·840 (0·051)			17·91	
	22-4-17__1		high	33·0	0·712 (0·042)	0·80 (0·28)	0·05	30·41	42·84
	22-4-17__2				0·772 (0·046)			29·88	
EU4	12-10-10__1	5	low	82·8	0·692 (0·023)	0·94 (0·14)*	11·10	17·26	40·74
	12-10-10__2				0·664 (0·022)			14·22	
	12-10-27__1		modal	73·1	0·726 (0·036)	0·85 (0·10)*	8·89	20·18	33·64
	12-10-27__2				0·794 (0·066)			23·53	
	12-10-15__1		high	62·4	0·683 (0·030)	0·83 (0·08)*	6·74	16·84	28·38
	12-10-15__2				0·715 (0·023)			19·93	

*Concentrations already presented by Shea *et al.* (2012).
[1]Sample names with '1' for most vesicular portion of the clast and '2' for the densest area.
[2]Idealized stratigraphic height; vertical position in meters of the eruptive unit relative to a hypothetical outcrop that would contain all units together.
[3]End-member of a 100-clast density histogram; one low-, one modal- and one high-density clast have been characterized texturally and geochemically.
[4]Clast vesicularity derived from density measurements.
[5]Water analyses with standard deviations. When the two textural domains display different H_2O concentrations, they are both presented; when values are similar to less than 0·1%, analyses are merged into a single value.
[6]Decompression rates as calculated by Shea *et al.* (2011). Because we show herein that P6 belonged to the white pumice family, its rates were recalculated with parameters similar to EU2.
[7]Leucite abundances as calculated using a chemical mass-balance model of crystallization.
[8]Leucite abundances as measured within 2D sections and SEM images of AD 79 pumice.

bridging or non-bridging oxygens) (e.g. Mercier *et al.*, 2009; Le Losq *et al.*, 2012); (2) a broad asymmetric peak in the high-frequency domain (~3400–3700 cm^{-1}), ascribed to the bending and stretching of H_2O and OH molecules (Zajacz *et al.*, 2005; Di Muro *et al.*, 2006). The entire spectral region encompassing the three low-frequency peaks is here labeled 'ASF' for aluminosilicate framework, and the asymmetric H_2O–OH band is simply labeled 'H_2O'.

To quantify H_2O in glasses, the intensity (I) or the area (A) of the ASF peaks and of the H_2O peak are typically measured, and a combination of external and internal calibrations are used (Mercier *et al.*, 2010). The 'external' calibration consists in normalizing A_{H_2O} or I_{H_2O} from the 'unknown' to that of a set of known standards with independently measured H_2O contents. The calibration slope of the standards is directly used to retrieve H_2O concentrations ($X^{(std.)}_{H_2O}$). In turn, the 'internal' calibration helps in avoiding instrument-specific laser and spectrometer excursions by normalizing the area of the water band $A^{(std.)}_{H_2O}$ over one or all three of the ASF bands $A^{(std.)}_{ASF}$. A calibration curve is then obtained by plotting $X^{(std.)}_{H_2O}$ vs $(A^{(std.)}_{H_2O}/A^{(std.)}_{ASF})$ and the water content of the unknown is

Table 2: Groundmass glass major element analyses

Eruptive unit	Sample		*n*	SiO_2	TiO_2	Al_2O_3	FeO	MnO	MgO	CaO	Na_2O	K_2O	P_2O_5	Total[1]
EU2	15-2-11__1	low	6	53·81	0·23	21·97	2·63	0·14	0·19	3·31	6·92	7·22	0·03	97·14
	15-2-11__2		6	55·42	0·25	22·54	2·58	0·15	0·16	3·39	7·12	7·78	0·04	100·14
	15-2-3__1	modal	6	54·60	0·23	22·32	2·43	0·12	0·16	3·52	6·73	8·04	0·20	99·01
	15-2-3__2		6	55·15	0·23	22·41	2·50	0·15	0·17	3·34	6·90	8·37	0·04	99·90
	15-2-5__1	high	6	54·86	0·22	22·36	2·40	0·12	0·16	2·93	6·57	9·17	0·03	99·45
	15-2-5__2		6	55·15	0·25	22·38	2·55	0·14	0·16	3·29	6·99	8·23	0·04	99·86
P1	26-1-5__1	low	5	53·14	0·37	20·89	3·57	0·15	0·47	4·61	6·01	7·07	0·10	97·07
	26-1-5__2		5	53·41	0·39	20·98	3·48	0·14	0·43	4·56	6·25	6·89	0·10	97·33
	26-1-7__1	modal	5	53·41	0·40	20·84	3·62	0·14	0·50	4·45	5·38	8·70	0·09	98·16
	26-1-7__2		5	52·92	0·39	20·67	3·61	0·13	0·52	4·33	5·08	8·89	0·11	97·27
	26-1-11__1	high	5	52·96	0·41	20·78	3·73	0·14	0·53	4·70	5·84	7·23	0·09	97·10
	26-1-11__2		5	52·69	0·42	20·75	3·92	0·15	0·53	4·98	6·41	6·27	0·10	96·94
EU3base	12-8-29__1	low	10	51·58	0·42	20·29	3·77	0·15	0·57	5·03	5·41	7·99	0·10	95·98
	12-8-29__2		10	51·44	0·41	20·55	3·83	0·15	0·54	5·09	5·47	7·74	0·07	95·95
	12-8-13__1	modal	10	52·64	0·44	20·41	4·15	0·18	0·58	5·46	6·52	6·40	0·11	97·60
	12-8-13__2		10	52·44	0·45	20·37	3·87	0·16	0·61	5·37	6·24	6·62	0·08	96·91
	12-8-37__1	high	10	52·05	0·43	20·90	3·93	0·15	0·53	4·97	7·11	5·96	0·09	96·83
	12-8-37__2		10	52·93	0·43	20·91	3·94	0·16	0·51	4·76	7·37	5·89	0·09	97·73
EU3max	12-9-42__1	low	139	53·93	0·45	20·40	3·95	0·14	0·65	4·82	4·95	8·95	0·10	98·96
	12-9-42__2		42	54·82	0·46	20·30	4·17	0·16	0·61	5·33	5·92	7·02	0·11	99·63
	12-9-16__1	modal	49	53·89	0·41	20·45	3·72	0·15	0·53	4·66	6·19	7·07	0·12	97·84
	12-9-16__2		12	53·29	0·41	20·70	3·83	0·15	0·55	5·01	6·30	6·47	0·13	97·52
	12-9-37__1	high	51	55·26	0·45	20·53	4·08	0·17	0·56	5·15	7·02	5·72	0·12	99·81
	12-9-37__2		39	54·61	0·46	20·37	3·97	0·17	0·53	5·13	7·46	5·45	0·11	99·07
P2	27-1-9__1	low	5	53·13	0·38	20·90	3·39	0·12	0·42	4·34	6·04	7·44	0·08	96·91
	27-1-9__2		5	53·54	0·35	21·14	3·21	0·15	0·34	4·55	6·20	7·35	0·09	97·59
	27-1-30__1	modal	5	53·32	0·37	20·98	3·53	0·13	0·47	4·33	5·68	8·18	0·08	97·72
	27-1-30__2		5	53·18	0·40	20·88	3·60	0·15	0·45	4·53	5·98	7·56	0·10	97·52
	27-1-4__1	high	7	53·63	0·40	21·09	3·77	0·16	0·43	4·99	6·81	5·95	0·10	98·12
	27-1-4__2		7	53·34	0·41	20·95	3·83	0·17	0·43	5·14	6·94	5·76	0·09	97·95
P3	28-1-32__1	low	5	53·49	0·41	20·93	3·75	0·13	0·55	4·53	5·60	8·29	0·10	98·45
	28-1-32__2		5	53·39	0·40	20·64	3·74	0·14	0·56	4·31	5·40	8·51	0·10	97·84
	28-1-12__1	modal	5	53·64	0·40	20·86	3·75	0·16	0·50	4·70	5·81	7·97	0·09	98·55
	28-1-12__2		5	53·74	0·39	20·97	3·79	0·14	0·50	4·52	5·80	7·90	0·07	98·49
	28-1-1__1	high	5	54·31	0·44	21·03	4·02	0·17	0·56	5·06	6·53	6·54	0·09	99·46
	28-1-1__2		5	54·14	0·44	20·98	4·15	0·17	0·58	5·29	6·58	6·40	0·11	99·59
P4	19-1-21__1	low	5	53·72	0·37	21·20	3·37	0·14	0·37	4·44	6·28	7·68	0·06	98·33
	19-1-21__2		6	53·49	0·39	21·17	3·48	0·14	0·39	4·85	6·45	6·97	0·09	98·19
	19-1-4__1	modal	5	53·26	0·46	20·49	4·11	0·14	0·57	5·16	5·83	7·20	0·15	98·04
	19-1-4__2		5	53·22	0·48	20·51	4·18	0·16	0·56	5·29	5·99	6·89	0·13	98·14
	19-1-10__1	high	5	53·73	0·46	20·73	4·03	0·14	0·57	4·80	5·75	7·94	0·09	98·87
	19-1-10__2		5	53·83	0·44	20·79	4·09	0·14	0·58	5·13	5·67	7·56	0·11	99·01

(continued)

Table 2: Continued

Eruptive unit	Sample		*n*	SiO_2	TiO_2	Al_2O_3	FeO	MnO	MgO	CaO	Na_2O	K_2O	P_2O_5	Total[1]
EU3top	20-1-31__1	low	5	53·56	0·40	20·69	3·73	0·14	0·52	4·47	5·28	8·56	0·11	98·09
	20-1-31__2		5	53·85	0·40	20·97	3·62	0·13	0·50	4·20	5·28	8·93	0·08	98·62
	20-1-4__1	modal	5	54·29	0·45	20·62	4·04	0·15	0·58	5·20	5·45	7·38	0·13	98·98
	20-1-4__2		5	53·68	0·45	20·57	4·01	0·15	0·56	5·01	5·30	7·74	0·11	98·26
	20-1-5__1	high	5	54·62	0·46	20·83	4·12	0·15	0·57	4·91	5·60	7·82	0·09	99·83
	20-1-5__2		5	55·14	0·48	20·99	4·22	0·16	0·59	5·03	6·48	6·44	0·10	100·33
P5	21-1-52__1	low	6	52·62	0·39	20·89	3·58	0·14	0·44	4·52	5·81	7·47	0·07	96·62
	21-1-52__2		6	53·19	0·37	20·89	3·59	0·14	0·45	4·74	6·05	7·18	0·07	97·36
	21-1-10__1	modal	7	53·24	0·38	20·93	3·58	0·14	0·44	4·41	5·93	7·79	0·08	97·61
	21-1-10__2		7	52·83	0·35	21·01	3·45	0·14	0·43	4·18	5·56	8·32	0·07	97·01
	21-1-2__1	high	10	53·59	0·39	21·27	3·63	0·14	0·46	4·44	6·35	6·86	0·09	97·87
	21-1-2__2		10	53·35	0·40	21·12	3·65	0·14	0·46	4·31	6·02	7·53	0·07	97·70
P6	22-4-8__1	low	20	53·77	0·18	23·02	2·12	0·14	0·10	3·10	7·27	7·80	0·02	98·21
	22-4-35__1	modal	10	53·75	0·20	23·36	2·45	0·16	0·13	3·86	8·08	6·17	0·02	98·98
	22-4-35__2		10	53·62	0·22	23·10	2·49	0·17	0·15	3·40	8·00	6·74	0·03	98·75
	22-4-17__1	high	10	54·69	0·26	23·31	3·43	0·26	0·13	2·65	12·91[2]	4·20	0·02	100·74
	22-4-17__2		10	54·17	0·27	23·32	3·36	0·27	0·14	2·56	12·68[2]	4·30	0·02	100·08
EU3base	12-10-10__1	low	10	51·87	0·36	20·94	3·40	0·13	0·44	4·94	6·09	7·05	0·21	96·10
	12-10-10__2		10	52·28	0·38	20·68	3·48	0·15	0·42	4·37	6·26	7·66	0·07	96·40
	12-10-27__1	modal	10	51·93	0·42	20·97	3·76	0·15	0·57	4·74	6·21	6·46	0·10	96·04
	12-10-27__2		10	51·02	0·37	20·85	3·48	0·15	0·38	4·76	6·98	5·79	0·07	94·65
	12-10-15__1	high	10	52·73	0·40	21·00	3·70	0·16	0·48	4·66	6·06	7·13	0·08	97·08
	12-10-15__2		10	53·14	0·40	21·10	3·86	0·16	0·48	5·00	6·38	6·51	0·06	97·81

[1]Totals do not take into account measured H_2O.
[2]Sample experienced Na loss and values reported include a correction. (See text for explanation.)

calculated from the empirically fit equation. This calibration is fairly straightforward, and, provided that the three peaks of the ASF band are used for internal calibration, appears to be composition-independent (Le Losq *et al.*, 2012). This is the strategy adopted here, and we generated our glass calibration curve using solubility experiments for phonolitic (Larsen, 2008) and rhyolitic (Devine *et al.*, 1995) compositions, as well as basaltic melt inclusions independently analyzed for H_2O (Kelley & Cottrell, 2012; J. F. Larsen & P. Wallace, personal communications) to test for compositional independence (Fig. 3b). Independent H_2O contents for these standards were all determined using FTIR, the precision and accuracy of which are estimated to be ~0·05–0·15 wt % and ~0·10–0·30 wt % respectively (Le Losq *et al.*, 2012; Shea *et al.*, 2012). The calibration standards define a narrow array, which we fitted with a second degree polynomial to retrieve H_2O concentrations from the area ratio A_{H_2O}/A_{ASF}. The average precision and accuracy for microRaman analysis are ~0·10 wt % and 0·30 wt % respectively, similar to values reported by Le Losq *et al.* (2012).

As in the study by Shea *et al.* (2012), all H_2O analyses were performed on a Witec Alpha300R confocal microscope of the University of Hawaii, using a 'green' laser (532 nm wavelength) at maximum power (5 mW) to maximize the signal-to-noise ratio. This setting imposed short counting times (~10–30 s) to avoid burning of epoxy-filled bubbles. The beam was focused through a ×100 objective on an ~1 μm spot, and laser power was periodically checked for drift. Raman spectra were collected in the 200–4000 cm^{-1} domain, and signal processing was performed using the 'SpeCTRa' (Spectral Correction Tools for Raman) Matlab routine (unpublished). This program allows the user to define anchor points on the glass spectrum, through which a polynomial is fitted; once the fitted baseline is subtracted, the program measures the ASF and H_2O areas. The user can also input a raw epoxy spectrum, allowing for subtraction of undesirable epoxy peaks. Two

Table 3: Melt inclusion major element, Cl and H_2O analyses

Sample	SiO_2	TiO_2	Al_2O_3	FeO	MnO	MgO	CaO	Na_2O	K_2O	P_2O_5	Cl	Total[1]	H_2O
Cl79_12-8-29_MI1	53·95	0·27	22·54	1·48	0·10	0·22	5·78	3·99[2]	5·87	0·44	0·67	95·29	4·98
Cl79_12-8-13_MI1	56·08	0·39	21·12	2·33	0·09	0·29	3·04	5·45[2]	8·92	0·06	0·53	98·28	5·55
Cl79_12-8-13_MI2	56·92	0·44	20·75	2·20	0·10	0·25	2·67	4·70[2]	8·59	0·05	0·43	97·10	5·54
Cl79_12-8-13_MI3	56·12	0·44	21·62	1·59	0·06	0·22	3·22	4·56[2]	8·48	0·43	0·53	97·27	5·99
Cl79_12-8-37_MI1	56·14	0·45	21·70	3·09	0·17	0·11	3·49	5·81[2]	7·80	0·03	0·68	99·47	4·55
Cl79_12-8-37_MI2	54·97	0·41	20·86	1·60	0·10	0·33	4·77	4·13[2]	7·58	0·11	0·62	95·49	4·80
Cl79_12-8-37_MI3	56·53	0·50	21·41	2·76	0·13	0·17	2·80	4·89[2]	8·72	0·12	0·73	98·77	2·59
Cl79_12-9-16_MI1	57·80	0·52	21·68	2·49	0·09	0·17	2·61	4·55[2]	9·20	0·07	0·52	99·70	3·55
Cl79_12-9-16_MI2	56·73	0·43	22·07	2·72	0·13	0·11	3·48	5·93[2]	9·09	0·08	0·66	101·44	3·61
Cl79_12-9-16_MI3	57·53	0·54	21·58	2·30	0·10	0·13	2·77	5·20[2]	9·32	0·09	0·60	100·17	3·25
Cl79_12-9-37_MI1	57·64	0·32	21·39	1·36	0·07	0·23	3·84	3·75[2]	7·12	0·12	0·50	96·34	6·34
Cl79_12-9-37_MI3	52·16	0·53	19·85	2·32	0·08	0·16	11·03	5·04[2]	7·25	0·11	0·62	99·14	4·07
Cl79_12-9-37_MI4	56·45	0·35	23·83	3·98	0·22	0·15	3·28	6·42	5·91	0·02	0·61	101·23	2·63
Cl79_12-9-42_MI1	54·99	0·35	21·08	2·38	0·11	0·12	3·09	5·56[2]	9·17	0·04	0·63	97·51	4·00
Cl79_15-2-5_MI1	55·16	0·52	20·90	2·87	0·12	0·51	4·53	5·88[2]	8·76	0·04	0·54	99·83	2·57
Cl79_15-2-3_MI1	56·18	0·30	22·36	2·37	0·12	0·11	2·74	5·70[2]	8·59	0·02	0·61	99·10	6·36
Cl79_15-2-3_MI2	56·64	0·35	21·95	2·18	0·10	0·14	2·78	4·94[2]	9·13	0·12	0·62	98·97	5·32
Cl79_15-2-3_MI3	57·01	0·39	21·30	2·28	0·09	0·11	2·92	4·93[2]	8·95	0·04	0·59	98·60	6·57
Cl79_15-2-3_MI4	56·69	0·39	21·15	1·97	0·09	0·15	3·26	4·87[2]	9·15	0·07	0·54	98·33	4·95
Cl79_15-2-3_MI5	56·70	0·39	21·47	2·25	0·08	0·11	2·90	4·47[2]	8·78	0·07	0·54	97·76	5·94
Cl79_15-2-3_MI6	56·69	0·41	21·55	2·13	0·08	0·12	2·70	6·25[2]	8·72	0·10	0·60	99·36	4·25
Cl79_15-2-3_MI7	55·91	0·45	21·58	2·41	0·12	0·15	3·02	6·17[2]	9·72	0·07	0·62	100·21	4·72
Cl79_15-2-11_MI1	57·25	0·21	21·08	2·53	0·14	0·08	3·00	4·88[2]	8·63	0·06	0·65	98·52	6·00
Cl79_22-4-8_MI3	57·02	0·20	24·05	2·57	0·14	0·08	2·59	6·15[2]	7·10	0·01	0·62	100·54	4·27
Cl79_22-4-17_MI1	56·47	0·29	24·39	3·51	0·18	0·18	2·45	7·13	5·92	0·01	0·60	101·13	2·30
Cl79_22-4-17_MI2	55·93	0·50	21·76	2·69	0·09	0·12	1·75	7·00[2]	9·16	0·08	0·58	99·66	4·18
Cl79_22-4-17_MI5	55·74	0·38	21·21	2·75	0·10	0·14	3·58	6·00	5·96	0·11	0·62	96·59	3·73
Cl79_22-4-35_MI1	56·54	0·38	21·49	1·86	0·07	0·13	2·77	4·81[2]	9·39	0·08	0·48	97·99	3·96
Cl79_12-10-10_MI1	55·16	0·41	21·61	2·53	0·11	0·16	3·35	5·61[2]	9·10	0·07	0·57	98·67	3·33
Cl79_12-10-15_MI1	54·71	0·48	21·14	3·08	0·11	0·19	2·66	4·85[2]	9·70	0·08	0·62	97·62	3·66
Cl79_12-10-15_MI2	54·81	0·49	20·99	2·56	0·10	0·18	2·53	5·02[2]	9·69	0·08	0·60	97·06	4·13

[1]Totals do not take into account H_2O.
[2]Sample experienced Na loss and values reported include a correction. (See text for explanation.)

types of measurements were performed; first, two sets of 6–15 analyses were carried out within the vesicular and the denser portions of each pumice clast (when these textural distinctions were present). Second, an H_2O profile was acquired across one sample displaying substantial textural heterogeneity (12-9-42 of EU3max) by measuring ~50 aligned glassy areas with the Raman microscope. To assess the variability of H_2O within each small glass area, 3–4 measurements were performed at each of the 50 'points' (totaling ~180 analyses). Two to three spots were also acquired within 32 melt inclusions ~10–60 μm in size.

Characterization of water degassing behavior using thermogravimetric analysis

The volatile content and degassing behavior of eight bulk samples (two pumices from EU3base, EU3top, EU4, and P6) were characterized using a TA Instruments SDT Q600 simultaneous differential scanning calorimetry–thermogravimetric analysis (DSC-TGA) instrument at Lancaster University, following methods described by Tuffen *et al.* (2010) and Denton *et al.* (2012). TGA can reveal distinct degassing signatures of magmatic and hydrated water in silicic pumices (Tuffen *et al.*, 2010, 2012) and dehydration patterns additionally provide information on the speciation

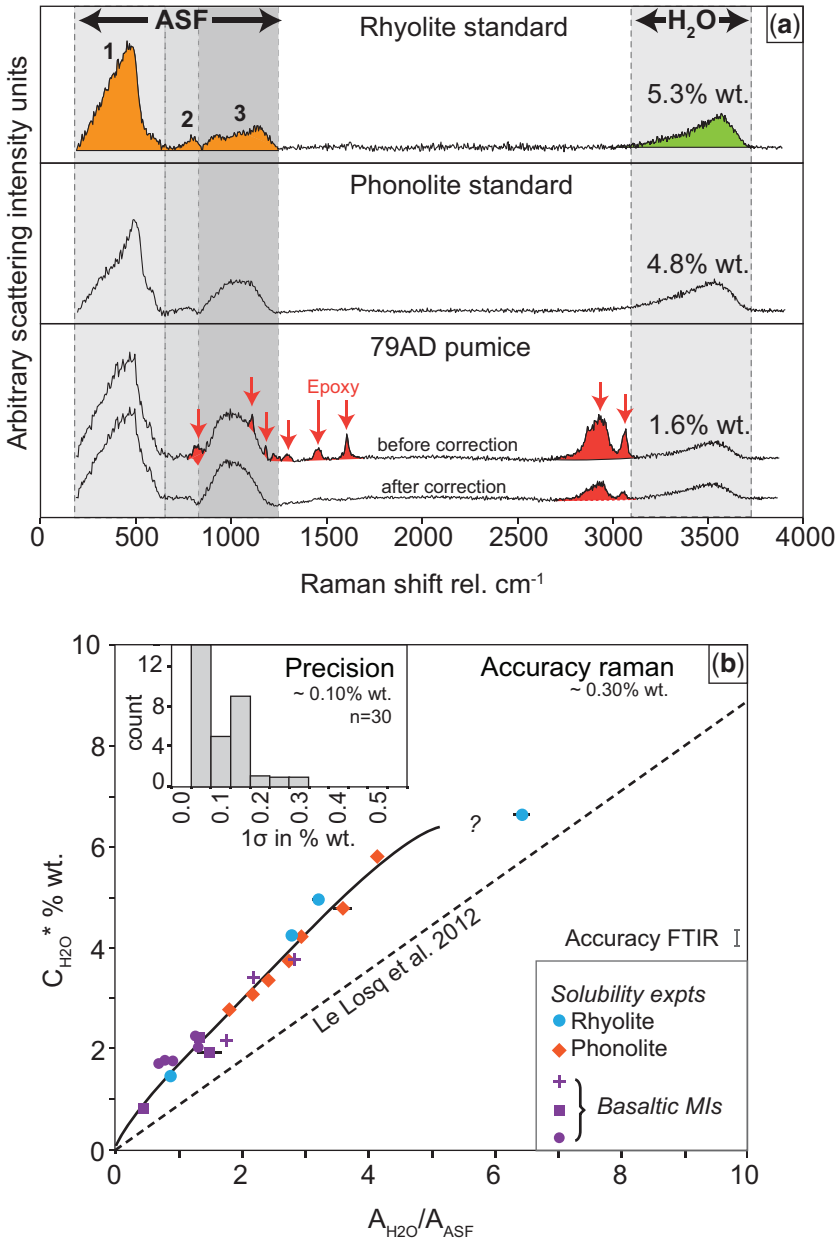

Fig. 3. Calibration of H_2O analyses using microRaman spectroscopy [modified from Shea *et al.* (2012)]. (a) Baseline-subtracted Raman spectra of various glasses (standards and natural pumice). Peaks related to the aluminosilicate framework (ASF) and H_2O are used for water quantification. Within natural pumice glasses, unwanted epoxy-related peaks are often present, and mostly affect the ASF region. A spectrum collected in pure epoxy can be used to correct for these undesired features. (b) Calibration curve obtained by analyzing standards from Devine *et al.* (1995) and Larsen (2008), as well as several previously characterized basaltic melt inclusions (Kelley & Cottrell, 2012; P. Wallace & J. F. Larsen, personal communications). The histogram in the inset illustrates the precision typically achieved within standard measurements, where each 'sample' ($n = 30$) is the standard deviation of 4–10 measurements. The calibration line of Le Losq *et al.* (2012) is shown for comparison.

of magmatic water (Denton *et al.*, 2012). Total volatile contents, as measured by TGA, agree well with the total of $H_2O + Cl + F + CO_2 + S$, as measured by micro-analytical techniques (Tuffen *et al.*, 2012). Powdered samples (125–500 μm grain size, ~50 mg) were placed in Al_2O_3 crucibles and heated within an oxygen-free, nitrogen-purged, platinum furnace to 1250°C, at 5°C min^{-1}, after an initial 10 h purge at 50°C to remove atmospheric contamination. The weight signal was calibrated using Al_2O_3 standards to correct for buoyant effects and beam growth drift. The furnace temperature was calibrated to better than ±3°C using six nickel–cobalt alloy Curie point standards.

Whole-rock results are presented as the abundance of microphenocrysts precluded separation of glass and crystalline components.

Quantification of Cl and other major elements using EMPA

Glass analyses of Cl and other major elements were obtained using a JEOL Hyperprobe JXA-8500F at the University of Hawaii. Large-scale textural variations (i.e. clasts within each eruptive unit) were measured spot by spot. Small-scale chemical variations were investigated in three steps. First, whenever textural variations within pumices were visible (e.g. darker vesicle-poor and lighter vesicle-rich areas), two sets of analyses were performed, one in the 'vesicular' zone and one in the 'dense' zone of the sample. Thus, in parallel with H_2O analyses, each set of three clasts has two sets of 5–10 chlorine and major element analyses (except for sample 22-4-8, which displayed no textural variations). Second, the same chemical profile as used for H_2O measurements (see above) was analyzed for Cl plus major elements. Third, four key locations across small-scale textural heterogeneities were selected for high spatial resolution chemical mapping (see below).

Point measurements were made on pumice glasses and MI using similar counting times but different beam diameters (6 and 2 μm in diameter respectively). Analyses were performed using a 15 keV accelerating voltage, 10 nA beam current, peak and background counting times of 10 s (Na), 15 s (Al), 20 s (Si, Mg), 30 s (Fe, Ca, P), 40 s (Ti, Mn), 50 s (K), and 80 s (Cl). Both natural glasses (VG-2, A99, Jarosewich *et al.*, 1980) and mineral standards were used for calibration. Glass standards were repeatedly analyzed to monitor any possible drift within measurements. Relative precision, inferred from these repeat analyses ($n = 5$–6) was on average 0·5% for FeO and CaO, 1% for SiO_2 and Al_2O_3, 1·5% for K_2O, TiO_2, FeO, and MgO, 3% for Na_2O and Cl, 10% for MnO, and 13% for P_2O_5. Accuracy for Cl was estimated by comparing values obtained in our measurements of VG-2 with those available from the GeoREM database, and is better than 0·006 % wt (absolute). Sodium loss was evaluated in several samples with phonolitic glass compositions with varying Na_2O (1·4–12 wt %) and H_2O (0·1–4·6 wt %) concentrations, and for three beam diameters (2, 6 and 10 μm). Na losses become significant when beam diameters of 2 μm are used, particularly in the more H_2O-rich samples (Fig. A3 in the Supplementary Data). Therefore, an Na correction was applied to melt inclusion analyses that were performed using a 2 μm beam. One H_2O-poor, but very Na-rich, sample (P6) also experienced Na loss during the analysis and was corrected for time-dependent intensity (Supplementary Data Fig. A3).

X-ray distribution maps for Cl (K_α), Si (K_α) and K (K_α) were generated using the same microprobe; higher beam currents (30–50 nA) and dwell times of 50–100 ms were employed. Although the resulting element images cannot be used in the same way as the higher precision point analyses, they provide an excellent spatial representation of compositional heterogeneity within a sample. To improve the signal-to-background ratio of these maps, Cl was measured using three of the five spectrometers (Si and K in the other two), and the resulting data were combined into a single 2D intensity matrix. The three intensity matrices for K, Si, and Cl were then merged into a RGB composite image, the abundance of these elements being represented by levels of red, green and blue respectively. To filter for the contributions of Cl-bearing epoxy, a back-scattered electron (BSE) image of the same area was used as a 'mask'. As vesicles and cracks appear black in BSE mode, they completely replace the areas filled by epoxy.

RESULTS

Large-scale variations

Major elements

Pumice glasses and melt inclusions show a wide compositional range in K_2O and more moderate variations in Na_2O and CaO (Fig. 4). Other elements display comparatively little variation. A simple mass-balance calculation involving the crystallization of leucite from the melt describes adequately the behavior of major oxides within the gray pumice glasses (see Supplementary Data for details). According to this model, melts crystallized anywhere between 12 and 43% from the starting composition, in good agreement with data obtained by textural measurements (15–40% of the vesicle-free volume, Shea *et al.*, 2012) (Fig. 5). White pumice (EU2) follows similar crystallization trends, but shifted towards more evolved compositions. Consistent with this crystallization model, K_2O can be used as a differentiation index for all glasses (Fig. 4, and Fig. A4 in the Supplementary Data). Interestingly, the three clasts from PDC unit P6 follow the white pumice array rather than the gray, suggesting that between the total collapse of the eruptive column (P5) and the onset of phreatomagmatic activity (EU4), white pumice magma was erupted in small volumes. The high-density clast from P6 is also unique in that it contains plagioclase and sodalite microlites, and has the lowest vesicularity measured in the AD 79 clasts (33%). In this sample, the crystallization of calcic plagioclase is expected to drive the melt Na_2O content up while depleting it in CaO and Al_2O_3 (Fig. 4b, d and f). Formation of sodalite should drive melt Na_2O down, but its compositional influence is probably masked by the more abundant plagioclase. From here on, we refer to P6 as white pumice even though it was erupted well after the main white pumice magma phase of the eruption.

Melt inclusions display a wider compositional spread than pumice glasses. For most elements, their compositions fall at the high-K_2O end of the white pumice glasses, and

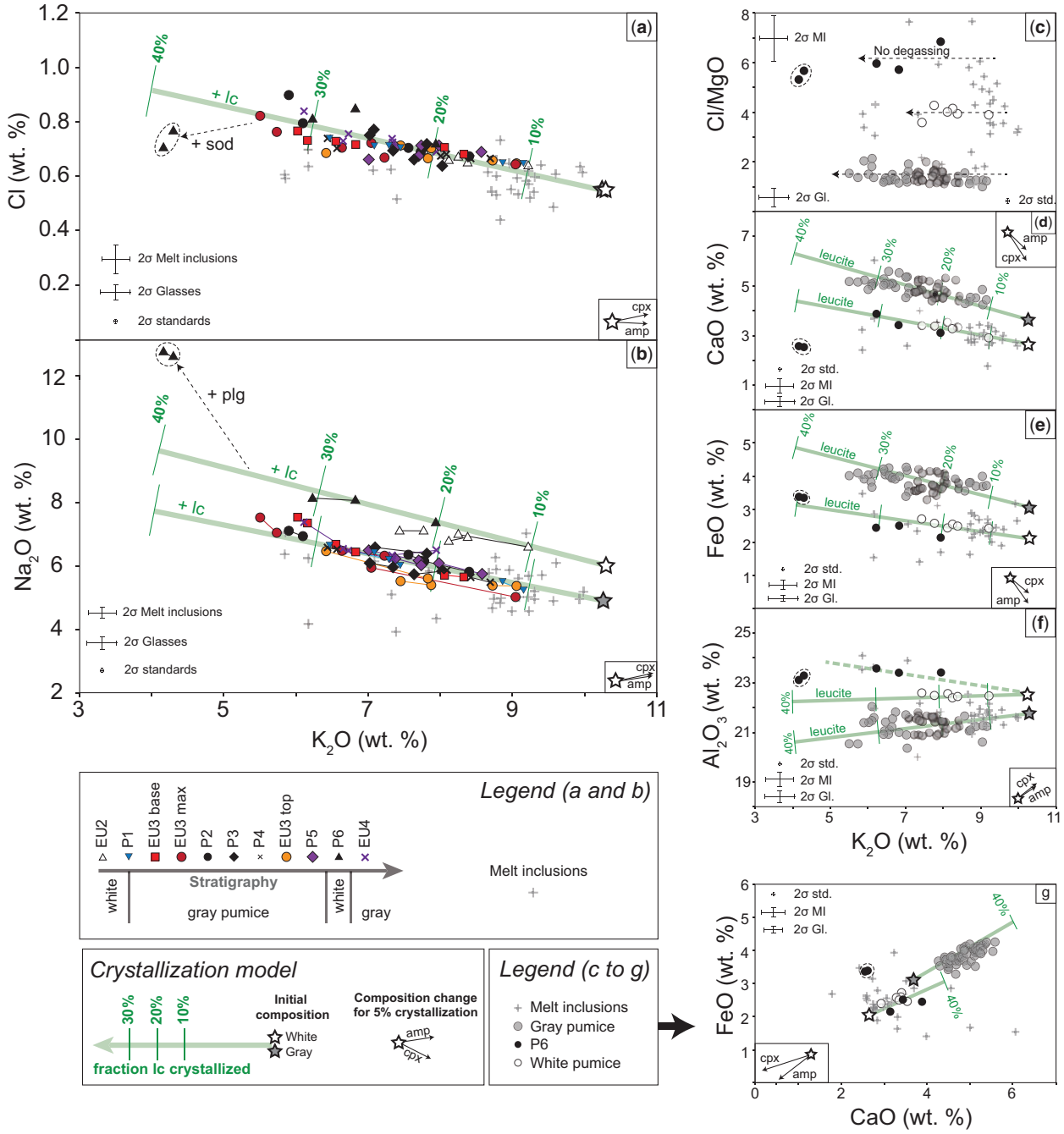

Fig. 4. Major element compositional variations of pumice glasses and melt inclusions. The continuous lines depict the chemical evolution of two starting melts (white and gray interstitial glass compositions, represented by white and gray stars respectively) crystallizing leucite (lc), as predicted by mass-balance calculations. K_2O is used as a differentiation index. In all diagrams, small black arrows show the extent of glass composition modification for crystallization of 5 vol. %. of other groundmass phases (cpx, clinopyroxene; amp, amphibole). Dotted oval outlines enclose P6, which is the only clast containing both sodalite (sod) and plagioclase (plg). It should be noted that the 'plus' signs imply phase addition by crystallization, without removal or fractionation. (a) Cl and (b) Na_2O track the leucite crystallization trend. In (b), analyses from two textural end-members (vesicular and dense) are connected by fine lines. (c) Ratios of incompatible elements Cl/MgO suggest an absence of Cl degassing during ascent of the AD 79 magmas. Plots (d)–(g) show that the leucite crystallization model works well for all oxides. P6 may display a separate evolution with respect to Al_2O_3 [dashed line in (f)]. In plots (c)–(g), pumice glasses are not distinguished based upon their stratigraphic location for simplicity. Standard deviations indicated are averaged for all glasses (2σ Gl.), melt inclusions (2σ MI), and known standards to assess reproducibility (2σ std.).

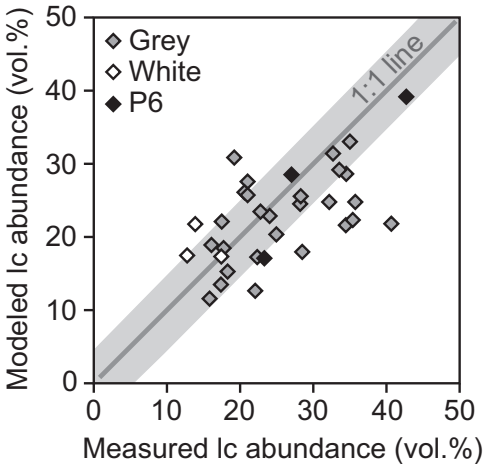

Fig. 5. Comparison between leucite content estimated by simple mass balance and leucite abundance measured through textural characterization. The standard deviation associated with textural measurements is shown as a wide array around the 1:1 line.

thus represent initial concentrations prior to crystallization of leucite. As a result, the high-K_2O end-member composition was chosen as initial concentrations for mass-balance calculations. On the other hand, some inclusions have low Na_2O (~4%) compared with what would be expected for a melt that is parent to the measured pumice glasses (~7% for white pumice); we interpret this to reflect insufficient correction of Na count-rate reduction during microprobe analysis.

Whole-rock volatile content and degassing behavior

The total volatile content of the eight representative Vesuvius pyroclasts analyzed (TVC_{TGA}) spans the range 1·9–4·1 wt %, and agrees well with the sum of H_2O and Cl determined by Raman analysis and EPMA: $TVC_{TGA} = 1{\cdot}1946(H_2O + Cl) + 1{\cdot}2536$; $R^2 = 0{\cdot}57$. The systematic offset (+1·25 wt %) is due to the contribution of F (0·25–0·75 wt %; Cioni, 2000; Balcone-Boissard *et al.*, 2008), CO_2 (predominantly present in carbonate inclusions) and the hydrous mineral analcime ($NaAlSi_2O_6.H_2O$), formed by partial transformation of leucite (e.g. Putnis *et al.*, 2007). The patterns of weight loss owing to devolatilization during heating (dTGA signal) reflect the concentration and speciation of volatile phases, together with their distance from powder surfaces (Tuffen *et al.*, 2012). Studies have shown that non-magmatic water generally escapes upon heating at low temperatures, whereas magmatic water and other volatiles are released at higher temperatures (e.g. Roulia *et al.*, 2006; Tuffen *et al.*, 2012). TGA of freshly erupted pumice from the 2008 Chaiten (Chile) eruption indicated minimal weight loss below 250°C (Tuffen *et al.*, 2010; Fig. 6a). TGA of Chaiten pumice experimentally rehydrated for 165 days showed that secondary water is released below ~250°C (Fig. 6a). Typical dTGA signals for six of the Vesuvian pyroclasts show little <250°C weight loss (typically 10% of the total volatile content, Fig. 6b and c). One dense pyroclast (20-1-5, with 55·7 vol % vesicularity) shows greater <250°C weight loss; this may reflect hydration, but the Raman H_2O value (0·24 wt %) makes it amongst the least water-rich of all pyroclasts analyzed; thus, it is unlikely that hydration would be reflected by the Raman-obtained H_2O value for this sample. The complexity in sample degassing behavior during TGA reflects contributions from various volatile-rich components (e.g. magmatic H_2O, carbonate inclusions providing CO_2 and H_2O, analcime, halogen species) that need to be carefully identified and quantified (e.g. Fig. 6b). Detailed analysis of these results will be provided in future work. Our key conclusion here is that TGA results support the notion that Raman H_2O values reflect magmatic rather than meteoric water.

Chlorine and water

Chlorine abundances range between 0·63 and 0·88% within pumice glasses, and between 0·43 and 0·73% in MI (Tables 1 and 3). Compared with previous studies, our pumice glass Cl concentrations overlap with those of Mues-Schumacher (1994), Cioni *et al.* (1995) and Signorelli and Capaccioni (1999), but differ from measurements made by Balcone-Boissard *et al.* (2008) (see Fig. A5 in the Supplementary Data). In the latter study, a calibration bias was invoked to explain the discrepancy between their Cl data and those of others. Therefore, herein, we assume that their calibration was different and make no specific comparisons with their Cl data (although their interpretations are discussed below).

On major element oxide plots, Cl increases linearly with progressive differentiation at the scale of all eruptive units (Fig. 4a). As for other elements, this behavior can be satisfactorily explained by the crystallization of leucite. Interestingly, there are no systematic differences between white and gray pumice, which suggests similar initial Cl concentrations. The low-vesicularity end-member of P6 forms an exception, with low Cl compared with what the crystallization model predicts. These lower concentrations probably result from sodalite crystallization, a phase containing ~6–7 wt % chlorine. On a plot of Cl/MgO vs K_2O, the data form horizontal arrays, suggesting a lack of strong Cl fractionation through degassing or crystallization (except for P6) within both the white and gray pumice magmas (Fig. 4c).

Measured H_2O concentrations vary in the range of ~0–2·1 wt % within pumice glasses, and ~2·3–6·6 wt % within MI (Tables 1 and 3). To characterize the combined behavior of water and chlorine, we compare our analyses with abundances predicted by the volatile solubility experiments of Iacono-Marziano *et al.* (2007) and Larsen (2008) for H_2O, and Signorelli & Carroll (2000) for Cl, all carried out using K-phonolite compositions similar to the gray and white pumice glasses. The Cl solubility model considers that the melt coexists with an H_2O-rich vapor

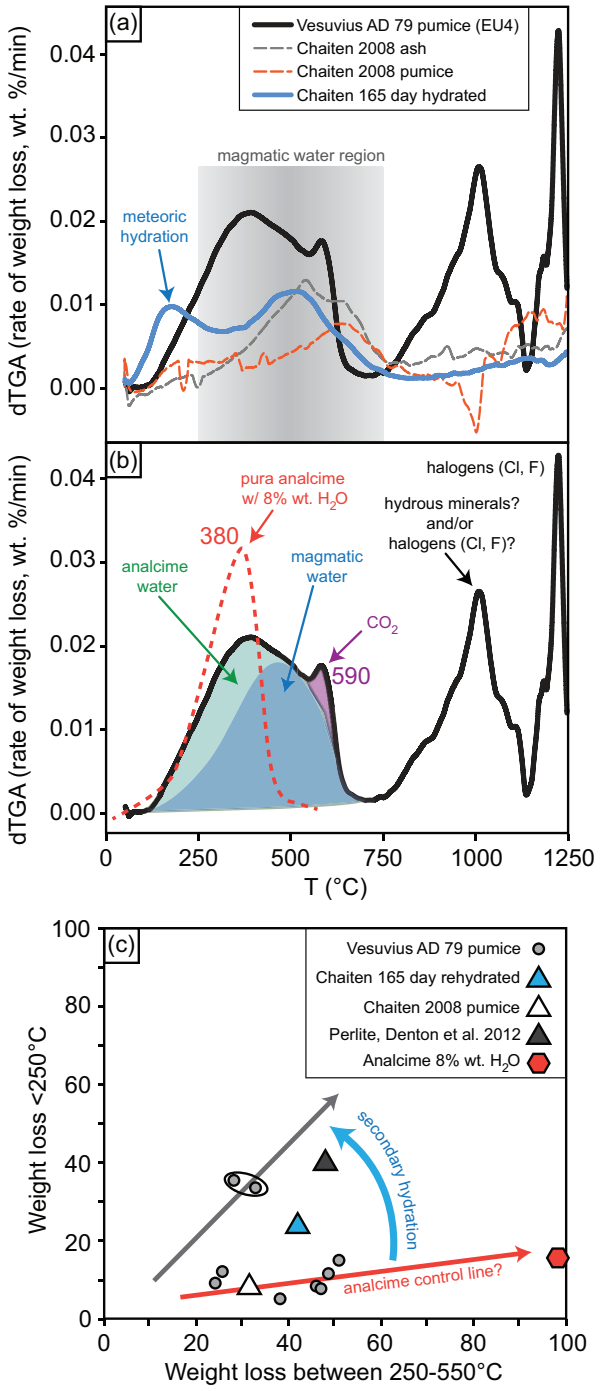

Fig. 6. Volatile release patterns from thermogravimetric analysis (TGA). (a) Comparison of TGA curves obtained from AD 79 Vesuvius pumice, 2008 Chaitén pumice, as well as a similar Chaitén pumice rehydrated under water for 165 days. The region typically attributed to release of magmatic water is wide (~250–750°C; Roulia *et al.*, 2006; Tuffen *et al.*, 2012), and peak positions for $T < 750$°C between Chaitén and Vesuvius pumices are variable. The hydrated pumice from Chaitén displays a peak associated with meteoric H_2O around 170°C, which is absent in other samples. (b) Interpretation of the volatile release pattern for Vesuvius pumice; the dotted curve corresponds to the H_2O-rich mineral analcime, with a peak around 380°C (Neuhoff & Wang, 2007), which probably contributes to the total H_2O (magmatic + analcime) release pattern in the 50–480°C domain. The peak at $T \sim 590$°C may represent CO_2 degassed from heating the carbonate inclusions within AD 79 pumices, and coincides with dTGA peak values found by Frost *et al.* (2009). High-temperature peaks are associated with the release of halogens (e.g. Tuffen *et al.*, 2012), with additional potential contributions from the hydrous minerals present in AD 79 pumices (amphibole and biotite). (c) Plot of mid-temperature vs low-temperature H_2O release. Most Vesuvius pumices plot on a line of minor low-temperature H_2O contribution, with some water being released by analcime. One sample shows some low-T degassing, suggesting possible rehydration, although Raman measurements do not reflect this.

phase, along with an immiscible hydrosaline Cl-rich brine. Our data define a fairly narrow, nearly vertical array (Fig. 7) with a small increase in Cl with decreasing H_2O. Compared with melt inclusion data from Cioni (2000), our MI data show some overlap with less scatter.

Small-scale variations

Major elements

Within sets of analyses performed in distinct textural areas of both white and gray pumice glasses (~6–10 analyses for each area), major elements display some notable variations. For instance, K_2O varies as much as 2%, Na_2O up to 1%, and CaO up to 0·5% (e.g. Fig. 4b). Other oxides show less variability. As at the larger scale, these second-order compositional variations can be explained by crystallization of various amounts of leucite. Therefore, areas with distinct textural and geochemical characteristics coexist at the scale of a single clast. This observation is confirmed by the sharp changes in K_2O along the chemical transect (Fig. 8), which correspond to visible textural differences.

Chlorine and water

Between 'dense' and 'vesicular' zones of a single thin section (EU3max, 12-9-42), absolute values of Cl vary by up to 2500 ppm, and water by up to ~1% wt (e.g. Fig. 8). The chemical transect acquired in this sample shows that Cl is anti-correlated with K_2O and H_2O (Fig. 8b and c). Hence, dense bands are richer in Cl and poorer in H_2O. Whereas Cl and K_2O show a fairly abrupt transition in their concentrations, H_2O varies more gradually across the textural heterogeneities. Also noteworthy is the presence of small compositional gaps when analyses are displayed in variation plots (Fig. 8c). As argued below, these gaps suggest that the shearing process was able to bring slightly different melts together.

More generally, the vesicular and dense textural domains analyzed in each of 33 clasts do not always show variations in water concentrations; in 60% of the pumices (20 out of 33), H_2O abundance is, within precision, indistinguishable between the two textural end-members (Fig. 7b and Table 1). In the other 40%, water is typically lower in the denser domains for each clast. In comparison, Cl concentrations are indistinguishable (within precision)

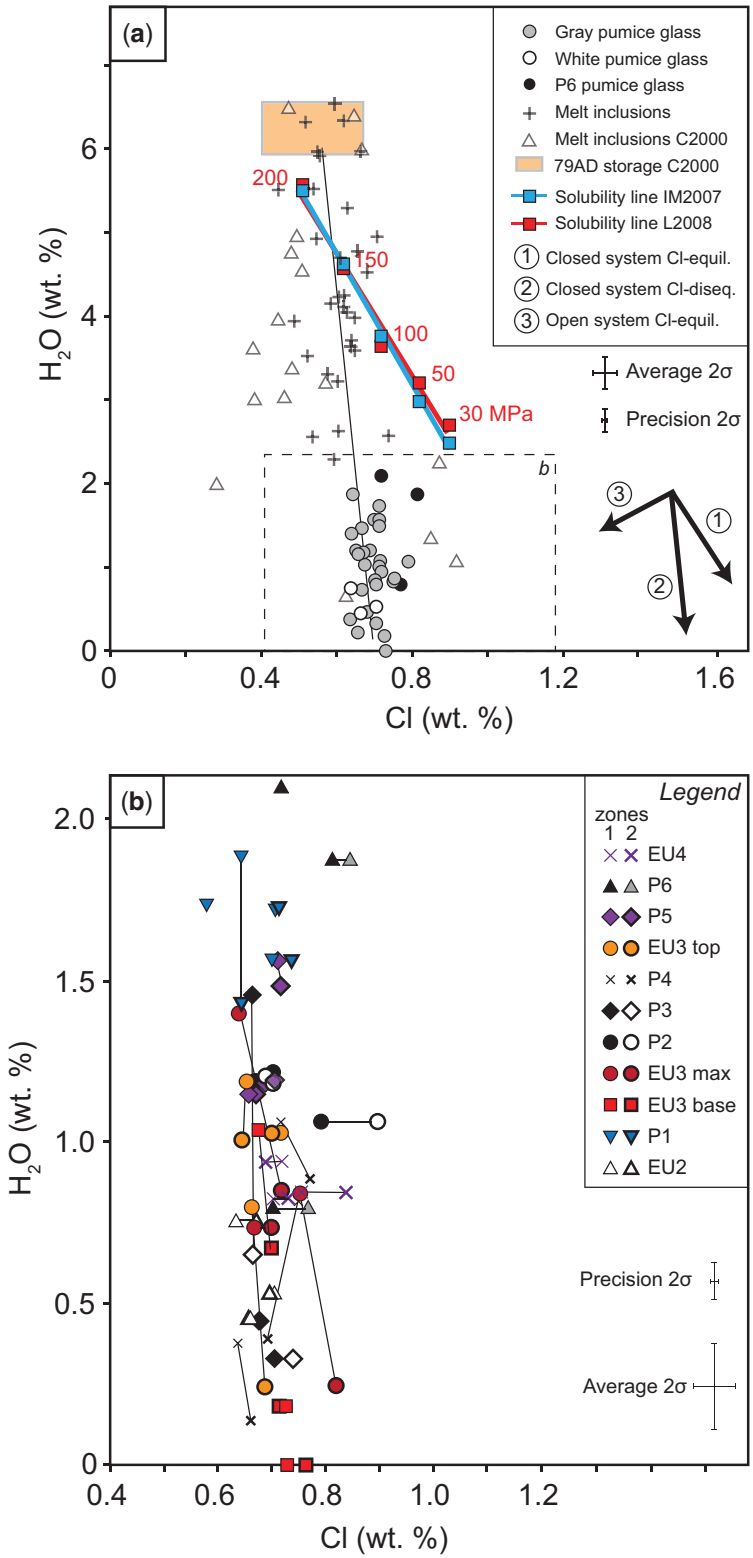

Fig. 7. Behavior of chlorine and water in pumice glasses and melt inclusions. (a) At the large scale, pumice glasses and melt inclusions form a near-vertical array with a slight increase in Cl with decreasing H_2O. Compositions at inferred storage conditions were determined by Cioni (2000) on the basis of melt inclusion data (shaded rectangle). Arrows illustrate the expected paths for models of (1) closed-system degassing at saturation with both a H_2O vapor phase and a Cl-rich brine, (2) disequilibrium H_2O degassing with no buffering by a Cl-rich brine and no Cl exsolution, and (3) open-system degassing with exsolution of both H_2O and Cl. (b) Close-up of the same data [dashed-line region in (a)], showing the distinction between clasts of different eruptive units. The pumice glasses each have two sets of analyses, one for the vesicular (zone 1) and one for the dense (zone 2) portions of the clast analyzed (connected by fine lines). Pumice standard deviations as well as estimated precisions are shown as averages in (a) and (b) for clarity. C2000, Cioni (2000); L2008, Larsen (2008); IM2007, Iacono-Marziano *et al.* (2007).

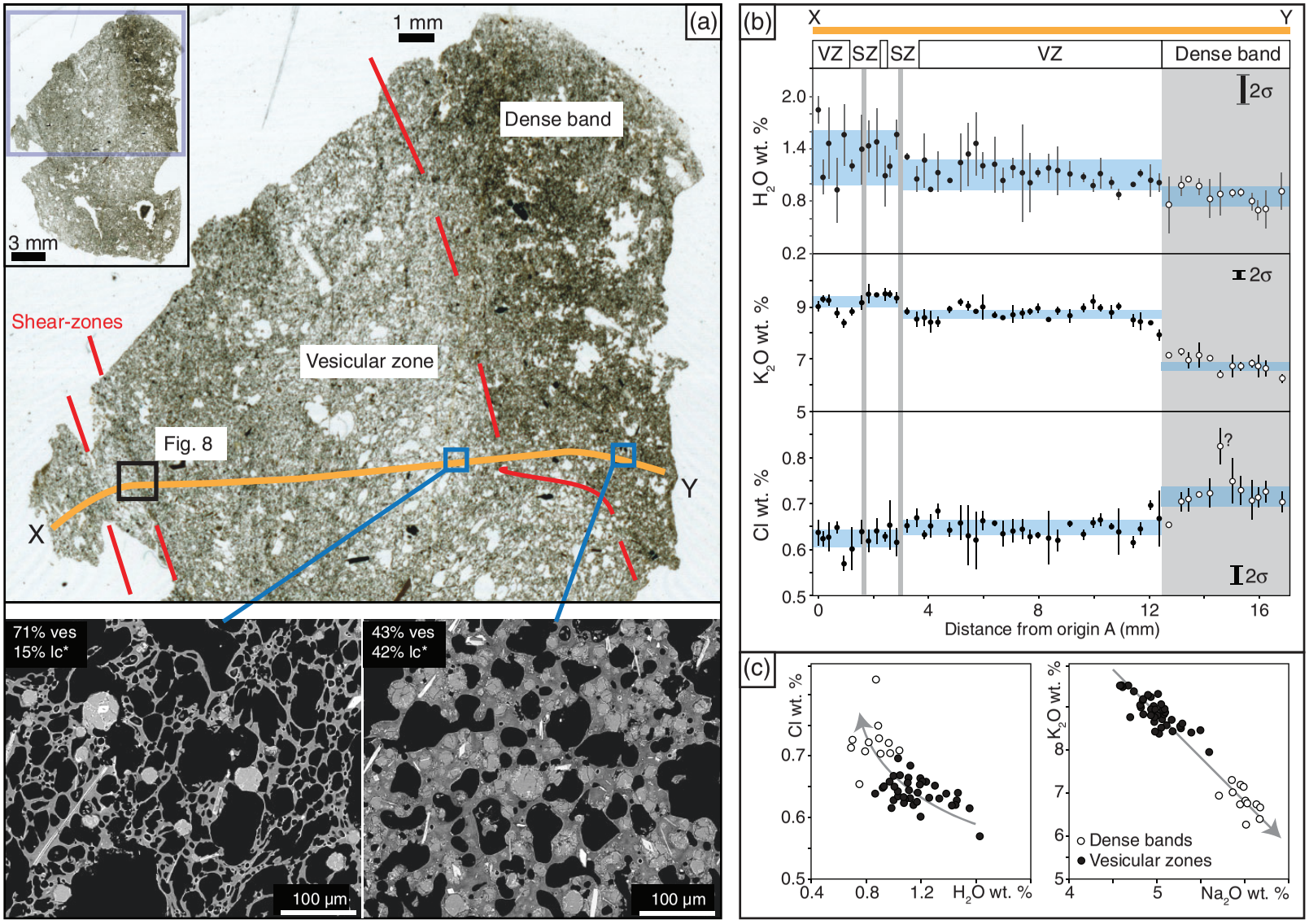

Fig. 8. (a) Scanned thin section displaying localized thin shear-zones and a thicker dense band on the right. Back-scattered secondary electron images below (locations shown as small rectangles) illustrate the striking textural difference between vesicular and dense portions. The round crystals are leucite; other microlites include pyroxene, amphibole, phlogopite and titanomagnetite. The black box shows the location of the element map in Fig. 9. (b) Chemical transect across X–Y, with some of the main textural features (VZ, vesicular zone; SZ, shear zone). Significant H_2O, K_2O and Cl variations occur within a single clast. The horizontal shaded arrays designate the inferred plateau values for the different elements, and their thickness on the *y*-axis corresponds to an average standard deviation. (c) Chemical variation plots illustrating the anti-correlation between H_2O and Cl concentrations, and the compositional gap between pumice areas that experienced different extents of degassing and were brought together by localized deformation (Na_2O vs K_2O). The light gray arrow shows the evolution of glass composition with increasing crystallization of leucite.

in 35% of clasts, and typically higher in denser zones within the majority of the samples (Fig. 8 and Table 2). When differences are observed in both volatiles within the same clast (nine out of 33), the denser portions of the pumices contain lower H_2O and higher Cl (positive slopes in Fig. 7b), with the exception of one clast.

An element map (Si, K, Cl) acquired within an ~0·2 mm wide vesicular shear-zone (see Fig. 8 for location) indicates that Cl has slightly lower concentrations within the deformation zone (Fig. 9). In contrast, within denser shear-zones or bands, Cl is enriched compared with the surrounding glass (element maps Figs 10 and 11). Qualitatively, denser portions of the samples also appear more leucite-rich.

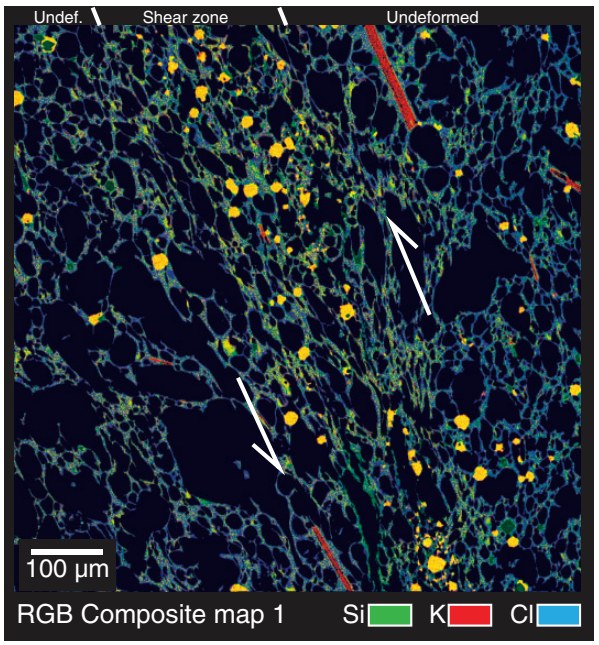

Fig. 9. Element map of a small shear-zone (from sample 12-9-42, EU3max, Fig. 8). Measured intensities of K, Si, and Cl are converted to levels of brightness and merged into a Red–Green–Blue image for viewing. Leucites are K-rich and appear bright orange, a few K-bearing micas are visible and appear darker orange, whereas small pyroxenes appear dark green. The pumice glass shows a transition from blue–green colors at the edges to a more greenish colour within the shear-zone, supporting a decrease in Cl. Vesicles are black.

DISCUSSION

In the first section of this discussion, we discuss the implications of our results for the AD 79 eruption, and more specifically, the evidence against syn-eruptive mixing–mingling as well as the lack of important Cl emissions during the eruption. In the second section, we discuss the virtues of Cl and H_2O as tracers of degassing in the context of highly explosive eruptions, the consequences of shear localization on degassing at the small and large scale, and some issues inherent to bulk volatile analyses.

Implications for the AD 79 eruption of Vesuvius

Did magma mingling or mixing occur syn-eruptively?

Sigurdsson *et al.* (1990) and Cioni *et al.* (1995) posited that mixing between the white pumice phonolitic magma and a mafic end-member occurred syn-eruptively. They based their findings largely on (1) variations in bulk pumice compositions (Ba and Sr) during the gray pumice magma phase, which they interpreted to reflect varying degrees of mixing between the two end-member magmas, and (2) the variability of groundmass glass compositions, which seemed to decrease with increasing stratigraphic height, suggesting an increasingly homogeneous melt composition with time.

In stark contrast to the above observations, our glass compositions appear to show that the white and gray pumice represent variable degrees of leucite crystallization from two distinct magma compositions, each initially homogeneous. If the interstitial melts had homogenized through time, the concentrations in most major elements would converge on variation diagrams (Fig. 4); instead, they show two distinct trends with little scatter around a leucite control line. Therefore, we propose that the gray pumice magma was efficiently homogenized before the eruption and that if syn-eruptive mixing occurred, it did not affect the interstitial melt compositions to a great extent. This observation is important because it validates the idea that compositional variations are related to degassing and degassing-induced crystallization, and not associated with various degrees of mingling and mixing of the white and gray pumice magmas (see the section 'Petrological and geochemical characteristics of AD 79 pumice', above). We note that the variations in Ba and Sr in bulk gray pumices with stratigraphic position, noted by Sigurdsson *et al.* (1990), could also be explained by varying abundances of sanidine incorporated during mixing with the white pumice magma. Sanidines commonly contain Ba and Sr in a wide range of concentrations (1000–12000 ppm and 200–2000 ppm respectively; e.g. Cioni *et al.*, 1995; Zellmer & Clavero, 2006) and are variably incorporated within the gray pumice.

Absence of chlorine exsolution during ascent of the AD 79 magmas

Previous volatile studies of the AD 79 eruptive products (Signorelli & Capaccioni, 1999; Cioni, 2000; Balcone-Boissard *et al.*, 2008, 2011) indicated that Cl contents are mostly constant within glasses or melt inclusions. Our analyses corroborate this finding, with additional evidence for a slight Cl increase in the melt during H_2O degassing (Fig. 7a). This increase results from the formation of leucite crystals during degassing, leaving the residual melt slightly Cl-enriched (Fig. 4a). Unlike Balcone-Boissard *et al.*

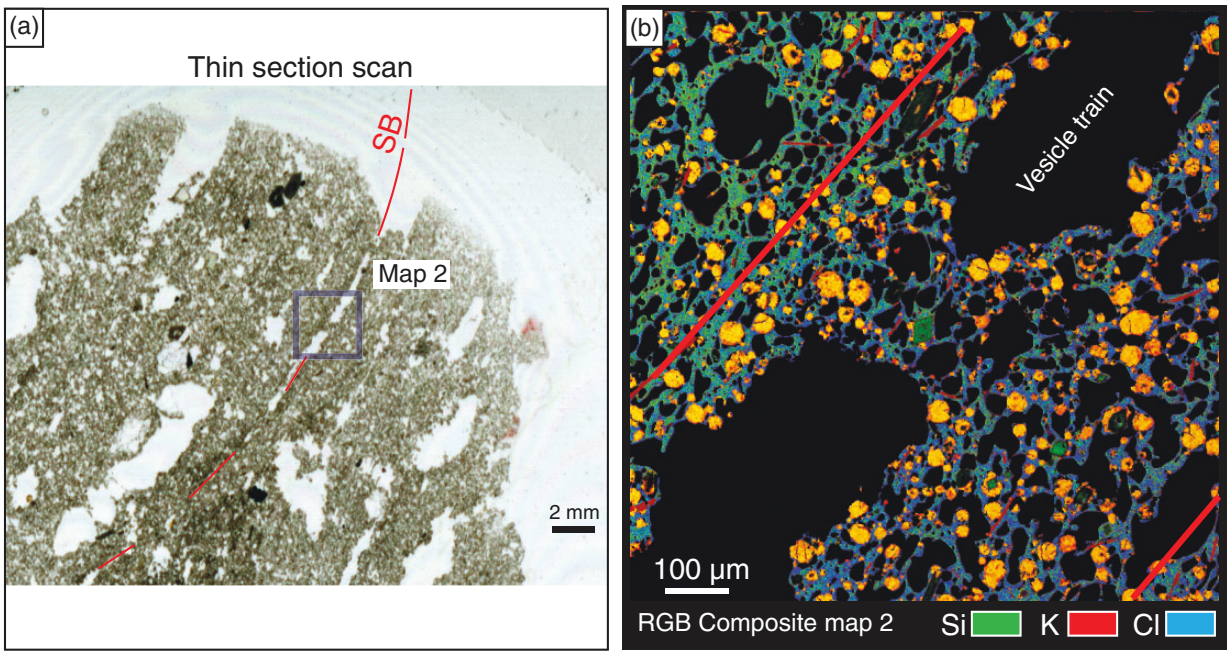

Fig. 10. (a) Thin section of pumice 12-9-16 (EU3max) displaying trains of deformed vesicles enclosed within denser strips of glass [interpreted to be a narrow shear-band (SB), shown in red]. (b) Element map obtained with the same configuration as in Fig. 9. The inferred shear-band SB is delimited by the two thick red lines. The high abundance of leucite within the band should be noted.

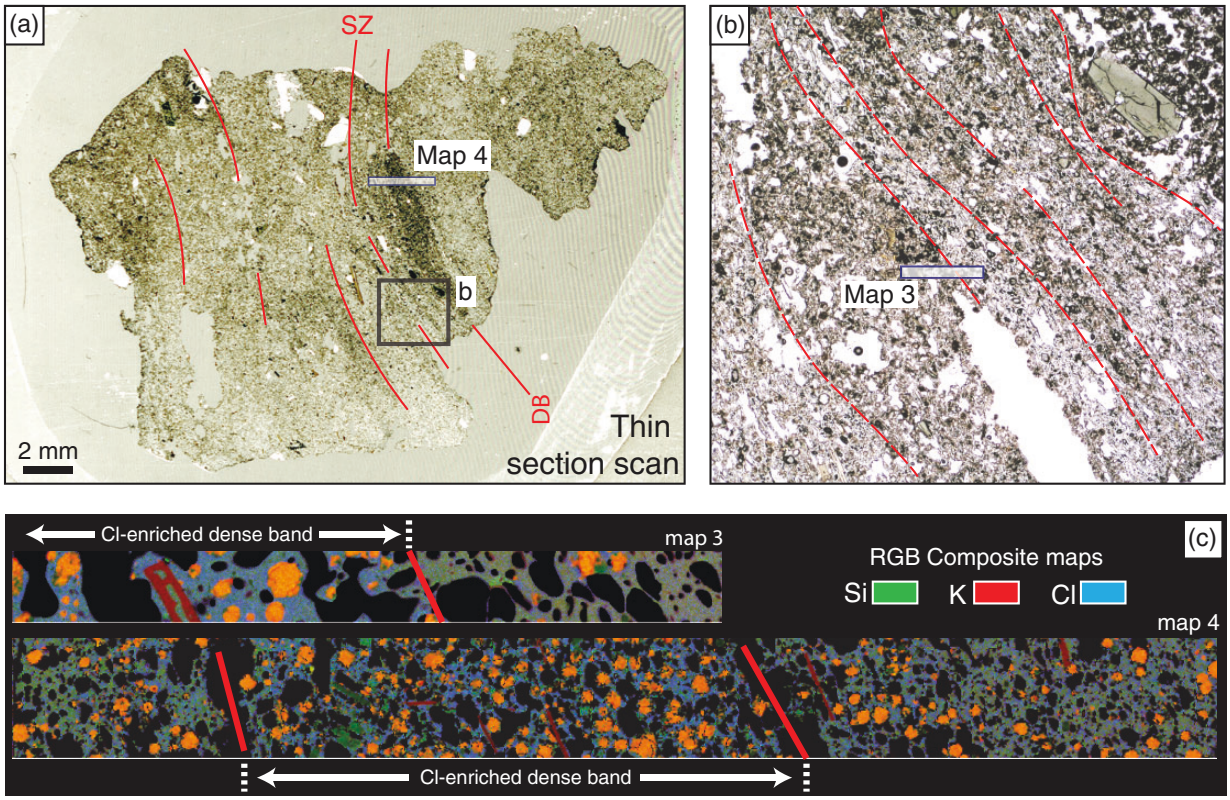

Fig. 11. (a) Thin section of pumice 19-1-10 (P4) showing textural heterogeneity, and (b) close-up of a region with abundant evidence for shearing. Map 3 was made at the boundary between a dense and a more vesicular portion of the clast, while map 4 traverses an entire discontinuous dense stretched lens. (c) Both maps show features reminiscent of map 2 (cf. Fig. 10), with denser section being enriched in Cl and enclosing higher abundances of leucites, and more vesicular areas showing a slight relative Cl depletion and fewer crystals.

(2008), who suggested that a portion of the gray pumice magma was undersaturated with respect to a Cl-rich hydrosaline fluid whereas most of the white pumice magma was saturated, we find no difference in Cl behavior between the gray and white magma. According to our data, most if not all of the AD 79 magmas were potentially saturated with such a fluid initially (Fig. 7a). During decompression, however, the slower diffusing Cl [diffusivity $D \sim 5 \times 10^{-13}\,m^2\,s^{-1}$ extrapolated from Balcone-Boissard *et al.* (2009) at $T = 1050^\circ C$] compared with a volatile such as H_2O ($D \sim 10^{-11}\,m^2\,s^{-1}$ at similar conditions) prevented any efficient extraction of Cl from the melt by exsolution. In addition, Cl concentrations did not follow solubility [increase in Cl within the melt as pressure decreases; Signorelli and Carroll (2000)], which essentially excludes the presence of a 'buffering' effect of a Cl-rich brine on the melt. Effectively, this implies that during the course of a highly explosive eruption such as Vesuvius AD 79, the output of Cl (typically in the form of HCl) to the atmosphere is probably minor. Most of the Cl is preserved within the erupted volcanic glass. The altogether non-volatile behavior of Cl during the AD 79 eruption confirms observations already made in the context of eruptions of similar or greater magnitude at Santorini (Greece) (Michaud *et al.*, 2000; Gertisser *et al.*, 2009).

Conduit-scale degassing variations: implications for the style and timing of magma ascent

Major elements and volatiles vary significantly within single units, and even within single clasts of the AD 79 eruption. At the scale of the conduit, this supports ideas of Shea *et al.* (2012) that there are lateral and vertical degassing gradients that vary through time. The notion that degassing heterogeneities at the conduit scale are responsible for the different types of clasts erupted at the surface has been proposed by various researchers in the context of explosive eruptions (e.g. Polacci *et al.*, 2001, 2003; Lautze and Houghton, 2007; Cimarelli *et al.*, 2010; Giachetti *et al.*, 2010). The data presented herein allow us to substantiate this idea through systematic measurements of volatiles in pumice glasses with a wide range of densities and textural attributes.

To a first order, the geochemical evolution of the AD 79 glasses appears to be well explained by the crystallization of leucite, as previously intimated by Signorelli & Capaccioni (1999) and Cioni (2000). Contrary to initial hypotheses that leucite grew during rapid magmatic ascent (e.g. Signorelli & Capaccioni, 1999), we previously advocated that leucite grew during a slower, earlier decompression stage of ascent, before rapid acceleration and fragmentation (Shea *et al.*, 2009). If H_2O degassing and leucite crystallization controlled melt composition, it follows that most of the geochemical attributes of these glasses may have been acquired during slow ascent in a lower conduit, or at the top of the reservoir. On the other hand, Cl–H_2O trends are in agreement with a generally rapid ascent style (see discussion below). Hence, the AD 79 magmas experienced non-linear ascent rates [as inferred from experimental studies of vesiculation by Shea *et al.* (2010*a*)] with low enough initial decompression rates, dP/dt, to allow for crystallization of leucite ($<0{\cdot}25\,MPa\,s^{-1}$), but high enough to prevent Cl exsolution (Fig. 12). The minimum decompression rate that is necessary to prevent Cl from degassing can be estimated using a simple diffusion model. We assume that to exsolve, an atom of Cl has to travel from its position in the melt to an existing melt–bubble boundary. This distance can be calculated using the average half-distance between bubbles $S_{half} = [3/(4\pi N_V)]^{1/3}$ [modified from Lyakhovsky *et al.* (1996)], where N_V is the bubble number density per melt volume. Because we consider that there are roughly two decompression stages ('slow' then 'fast'), we calculate S_{half} using two different values of N_V; a number density $N_V = 5 \times 10^{13}\,m^{-3}$ corresponding to the large bubble populations inferred to have formed at depth during slow decompression, and a number density $N_V = 10^{15}\,m^{-3}$ associated with small bubbles that form during accelerating decompression (values averaged for all gray pumice samples) (Shea *et al.*, 2010*a*; unpublished data). The time needed for Cl to diffuse to the melt–bubble boundary can then be calculated as $t = (S_{half})^2/D_{Cl}$, where D_{Cl} is the diffusivity. At a temperature $T = 1050^\circ C$, the diffusivity $D_{Cl} = 4{\cdot}5 \times 10^{-13}\,m^2\,s^{-1}$ [calculated from Balcone-Boissard *et al.* (2009)], which yields $t = 630$ s and $t = 86$ s for diffusion of Cl during the slow and rapid phases of ascent respectively. We can assume that the magma was decompressed by 150–200 MPa from the reservoir to fragmentation (e.g. Balcone-Boissard *et al.*, 2008; Shea *et al.*, 2010a) and that most leucite grew during a slow decompression stage at pressures of ~100 MPa (Shea *et al.*, 2009) (see Fig. 12b). Thus, we can infer that the total slow decompression stage was at least 50 MPa, and that the fast decompression was 100 MPa. In combination with the calculated minimum timescales for Cl diffusion, this simplified two-stage ascent model yields minimum 'integrated' decompression rates $dP/dt = 0{\cdot}08\,MPa\,s^{-1}$ and $dP/dt = 1{\cdot}16\,MPa\,s^{-1}$ for the gray pumice magma. Hence, the initial slower decompression rates that favored leucite growth were effectively between 0·08 and $0{\cdot}25\,MPa\,s^{-1}$, whereas the fast decompression rates reached a minimum of $1{\cdot}16\,MPa\,s^{-1}$. The latter value for minimum dP/dt attained during fast ascent is consistent with the rates calculated by Shea *et al.* (2011, 2012) using natural samples from gray pumice magma units, which are all above $2{\cdot}3\,MPa\,s^{-1}$ (Fig. 12a).

Similar calculations for H_2O need to account for the influence of degassing and decreasing water on diffusivity; as in the study by Shea *et al.* (2011), we use diffusivities of $D_{H_2O} \sim 10^{-11}\,m^2\,s^{-1}$ for initial slow ascent, and values five times lower for fast ascent when the melts have lost ~75%

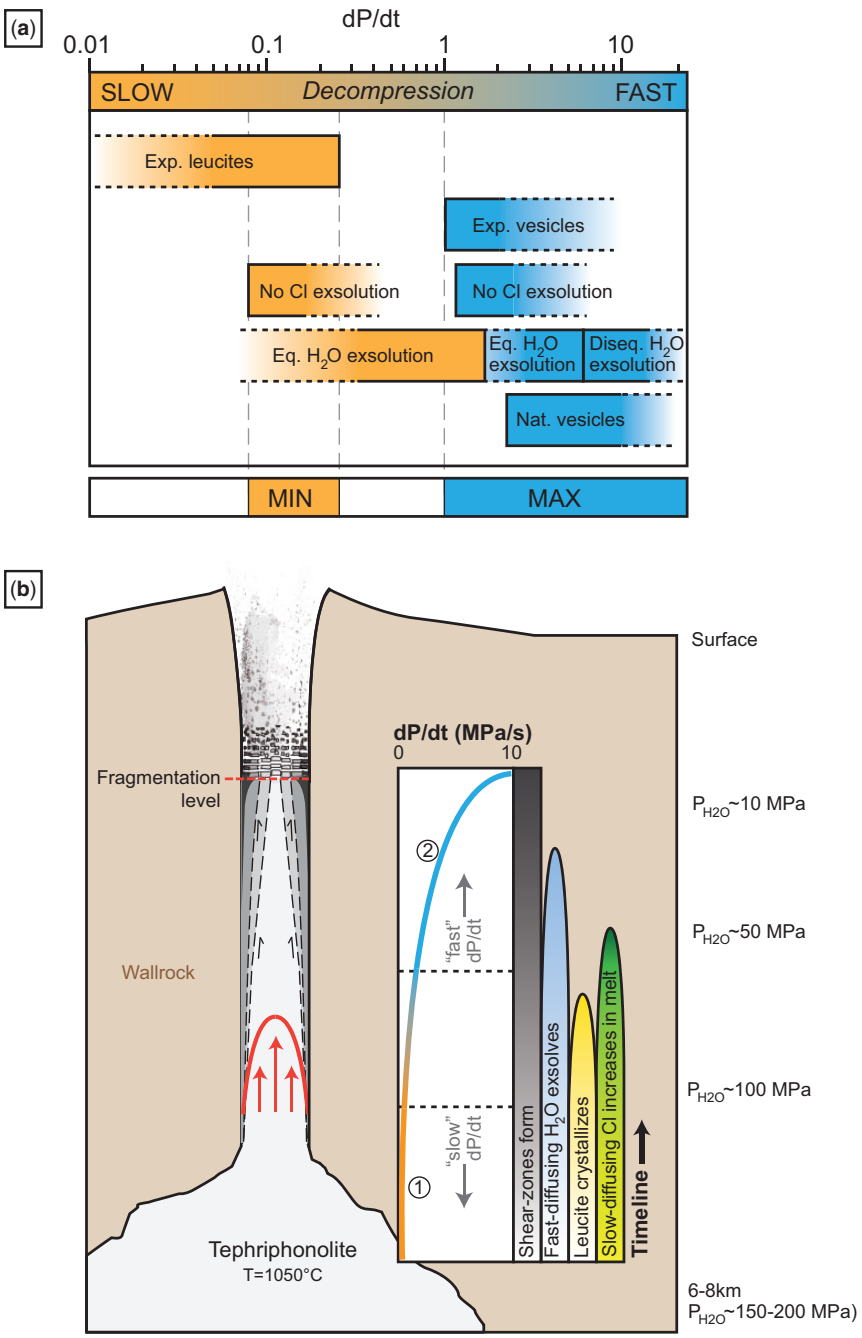

Fig. 12. (a) Constraints on magma decompression rates during the AD 79 eruption. Leucite crystallization experiments constrain the slower portion of ascent to decompression rates <0·25 MPa s^{-1} (labeled 'Exp. leucites'). Previous vesiculation experiments support minimum decompression rates of 1 MPa s^{-1} ('Exp. vesicles'). Cl diffusion constrains minimum dP/dt of 0·08 and 1·16 MPa s^{-1} to inhibit Cl exsolution during the slow and fast stages of ascent respectively ('No Cl exsolution'). A similar calculation for H_2O requires maximum dP/dt of 1·8 and 5·7 MPa s^{-1} to allow for equilibrium exsolution ('Eq. H_2O exsolution'). At higher decompression rates, disequilibrium H_2O degassing occurs ('Diseq. H_2O exsolution'), maintaining high residual H_2O concentrations within the AD 79 pumice. Decompression rates for AD 79 gray pumice yield dP/dt > 2·3 MPa s^{-1} ('Nat. vesicles') [see Shea *et al.* (2012) for details]. The 'MIN' and 'MAX' regions at the bottom summarize the dP/dt ranges inferred for the slowest and fastest stages of ascent. (b) Simplified sketch of how the non-linear, accelerating ascent style affected magma properties during the eruption. (1) The initial ascent phase was slow enough for H_2O to efficiently exsolve and leucite to crystallize, but fast enough to prevent Cl exsolution. (2) The second, rapid ascent stage resulted in the high bubble number densities measured in natural samples. Equilibrium H_2O exsolution was essentially possible until dP/dt became too high, and most leucite crystallized earlier in the ascent history. Because Cl did not exsolve during either slow or fast ascent, its concentration in the residual melt increased with H_2O degassing and leucite crystallization. The gray magma homogenized prior to ascent in the conduit, and, owing to lateral velocity gradients (continuous curve), strain localized near the conduit margins (darker gray colors illustrate denser magma portions).

of their H_2O. These diffusivities yield maximum decompression rates of 1·8 MPa s^{-1} and 5·2 MPa s^{-1} for efficient exsolution of water during the slow and fast ascent stages respectively (Fig. 12a). The average decompression rates are about 6 MPa s^{-1} for gray pumice (Shea *et al.*, 2011, 2012), whereas the fastest dP/dt estimated for this eruption is about 13 MPa s^{-1}. Hence, despite the fact that H_2O was extracted substantially from the melt during ascent, a certain amount remained in the melt, which is why we measure 2% H_2O within some glasses. Although there are uncertainties in such simplified models, they illustrate well the notion that kinetic effects can account for the lack of Cl degassing compared with H_2O.

Scales of degassing during explosive eruptions

Water and chlorine: macro- to micro-tracers of degassing

The near-vertical trend on a Cl–H_2O diagram (Fig. 7a) strongly diverges from the solubility lines calculated from Larsen (2008) and Iacono-Marziano *et al.* (2007) (water), and from the three-phase (melt + vapor + brine) solubility curve of Signorelli & Carroll (2000) (chlorine). Despite the scatter displayed by melt inclusion data, the departure of natural samples from the solubility line appears to start at around 125–200 MPa. Clearly, ascending magmas did not maintain solubility concentrations of Cl within a melt + vapor + brine system as H_2O was exsolving. We conclude that for the samples analyzed, there was no aqueous brine coexisting with the melt during ascent. If the melt Cl content was not buffered by a separate hydrosaline phase, Cl did not degas efficiently either, as there is no decrease in Cl with decreasing H_2O.

Along with data for three melt inclusions from Cioni (2000), three other MI from our dataset show H_2O abundances higher than the experimentally predicted solubility. Perhaps at high pressures (>125–150 MPa), CO_2 may have been present in the dissolved volatile phase (Cioni, 2000; Scaillet *et al.*, 2008), a species that is not accounted for in the solubility models and may affect pressure estimates at fixed H_2O contents. In all cases, at pressures lower than $P_{H_2O} = 125$ MPa, the melt Cl content increased only slightly but Cl was unable to degas or keep in equilibrium with solubility.

In general, H_2O can be considered a good tracer of magma ascent and degassing history at the large scale as it diffuses rapidly. Cl, on the other hand, diffuses more slowly, effectively behaves like an incompatible element, and merely increases as a result of H_2O loss and the ensuing crystallization of leucite (in the absence of a buffering hydrosaline fluid phase). Consequently, Cl could also hypothetically be a useful 'residual' tracer of H_2O degassing at the large scale. There is, however, a fairly wide array of Cl concentrations with decreasing H_2O among the various AD 79 units (Fig. 7). Considering that EMPA in this study was tailored for Cl (i.e. both high precision and accuracy) we cannot attribute this scatter to analytical uncertainty. A possible explanation for the dispersion of the Cl data is that each set of pyroclasts may have followed a slightly different degassing and leucite crystallization path before quenching occurred (see Fig. 13 for details). In summary, Cl analyses yield valuable first-order estimates of the style of ascent (equilibrium vs disequilibrium), but caution should be exercised when interpreting scattered halogen data to decipher volatile behavior at the large scale, as their concentrations are highly sensitive to H_2O degassing and crystallization at the small scale.

In fact, the chemical profile and maps (Figs 8–11) indicate that Cl can be used more efficiently to fingerprint clast- to submillimeter-scale degassing heterogeneities, because within a given pyroclast, the volatile behavior can be assumed to correspond to a single degassing trajectory (see Fig. 13). Notwithstanding the higher uncertainty inherent in H_2O measurements using Raman spectroscopy, the water concentration profile decreases gradually across the dense band boundary, whereas Cl shows a more abrupt transition (Fig. 8). Assuming that this boundary represents an association of relatively H_2O-depleted melt on one side and H_2O-enriched melt on the other, the difference in profile shape could be related to re-equilibration timescales; Cl did not have enough time to significantly diffuse from the time these two melts were in contact, whereas faster diffusing H_2O would have begun re-equilibrating. Even so, the timescales of ascent were probably too short for complete re-equilibration to have occurred. On chemical maps of other samples containing shear-bands composed of denser pumice (Figs 10 and 11), the apparent relationship between texture and Cl abundance is confirmed; denser zones have higher Cl, which means that they have probably degassed H_2O to a larger extent (e.g. Fig. 8b and c), and thereby crystallized more leucite. The chemical map of a 'young' shear-zone shows that in certain cases, this relationship is reversed (Fig. 9), with Cl being depleted within the localized deformation zone; a possible explanation for this is given below.

Overall, although high spatial resolution measurements of H_2O are becoming possible with tools such as Raman spectroscopy, Cl can also prove an excellent tracer of degassing owing to its incompatible behavior. Cl is incorporated into the structure of only apatite, micas or sodalite, which occur only in small abundances in these types of samples. Furthermore, the partition coefficient between melt and these minerals is too close to unity to truly affect melt composition (except for sodalite, which is present in only one sample). Second, there seems to be a direct link between textural heterogeneities and volatile contents, a conclusion that is not so surprising, but that remains to be developed further to understand magmatic ascent. Below,

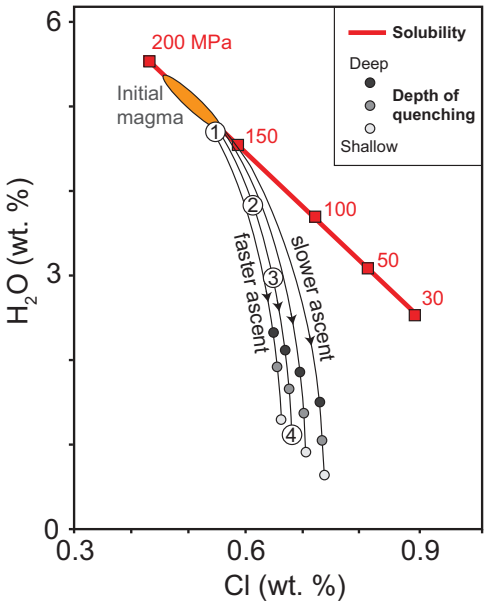

Fig. 13. Hypothetical model for the variability of volatile concentrations within the AD 79 pyroclasts. The plot shows possible evolutions for different portions of magma ascending at variable rates. An initial magma (shaded oval) residing at $P = 150$–200 MPa is decompressed non-linearly (see Fig. 12). During initial slow ascent, the magma composition tracks H_2O and Cl solubility (1), but gradually departs from equilibrium concentrations as ascent rates increase (2). H_2O degasses, even at fast ascent rates, whereas Cl is more sluggish, resulting in significant departure from solubility and an increasingly vertical trend (3). The final volatile contents of a pyroclast glass (4) vary as a function of the depth at which it was fragmented and quenched (shown as circles with three shades of grey). The fine black curves illustrate that since ascent and decompression rates vary between eruptive phases (Shea *et al.*, 2012), faster ascending magmas will tend to diverge from solubility earlier than slower ascending magmas. Furthermore, the extent to which leucite can crystallize in response to H_2O loss also controls the slope of the depicted curves. This combined behavior (degassing + crystallization) explains the variability in H_2O and Cl observed at the scale of the entire eruption (e.g. Fig. 7) (see text for details). As discussed in the text, Cl is much more useful to decipher the degassing history within a single pyroclast (i.e. at the microscale) as the corresponding magma volume is small and can be assumed to represent one trajectory within this type of plot.

we provide a conceptual model of degassing at the small scale, and highlight the importance of shear-zones in generating textural heterogeneity at the large scale.

The role and evolution of magma shearing during explosive eruptions

Evidence of shearing is omnipresent within the products of explosive eruptions. In deposits from the 37 ka bp Campanian Ignimbrite eruption (Campi Flegrei, Italy), shearing processes during magma ascent are expressed as tube pumices; these make up a little under 10% in number of the total pumices collected (Polacci *et al.*, 2003). These units also contain flattened or 'foliated' pumices, similar to those observed in deposits from other eruptions (e.g. Ramadas caldera, Martí *et al.*, 1999; Pinatubo 1991, Polacci *et al.*, 2001; Quilotoa 800 years bp, Rosi *et al.*, 2004). At Vesuvius, evidence for shearing is more subtle and takes the form of thin shear-zones with elongate vesicles, shear-bands that are typically denser and wider, or deformed trains of vesicles. Such micro-scale features are also recognized in silicic pumices from other locations (e.g. Wright & Weinberg, 2009).

By definition, shear-zones accommodate lateral velocity gradients, and we postulated in a previous detailed textural investigation of the AD 79 pumice that such velocity gradients generate lateral density gradients within the magma at the conduit scale (Shea *et al.*, 2012). The gradients are in turn expressed at the surface as pumice clasts with varying vesicularity or density. Hence, there should be a direct link between the formation of shear-zones, even at the small scale, and magma degassing during ascent. In a previous study (Shea *et al.*, 2012), we provided a hypothetical model of shear-zone formation and evolution, which was solely based on observed vesicle textures. The geochemical data given in the present contribution provide some groundwork to understand the linkage between these textures and degassing processes, and a new improved model for the formation and evolution of shear localization can be proposed (Fig. 14).

(1) A portion of undeformed magma (Fig. 14a) with spatially uniform chemical composition, vesicle distribution and crystal content starts to ascend and is progressively sheared to accommodate velocity differences (Fig. 14b). Reorganization of melt along planes near-parallel to the shear direction may facilitate the migration and exsolution of H_2O towards the zone of maximum strain. This H_2O enrichment within 'young' shear-zones results in an apparent lowering of Cl concentrations (i.e. a mass-balance effect) at these locations (Fig. 9).

(2) More vesicles are being deformed in the region of maximum strain, leading to coalescence and an increase in connectivity until bubbles collapse and outgassing occurs (Fig. 14c). By this stage, leucite crystallization progresses further with decreasing H_2O content in the melt. The distribution of volatiles at this stage could be similar to that observed in the Cl map in Fig. 10 (i.e. enrichment of Cl within the shear-zone and, by extrapolation of our results, a depletion of H_2O). Potentially, H_2O may concentrate at the very edges of the shear-zone, where the newly deforming melt is still volatile-rich. The chemical map in Fig. 10 does not display evidence for this phenomenon (concentration of water at the edges marked by a clear Cl decrease) but signal resolution may be too low to detect such a feature, or some diffusive re-equilibration may have occurred.

(3) If strain localizes elsewhere (potentially a result of strain hardening) and the shear-zone is abandoned,

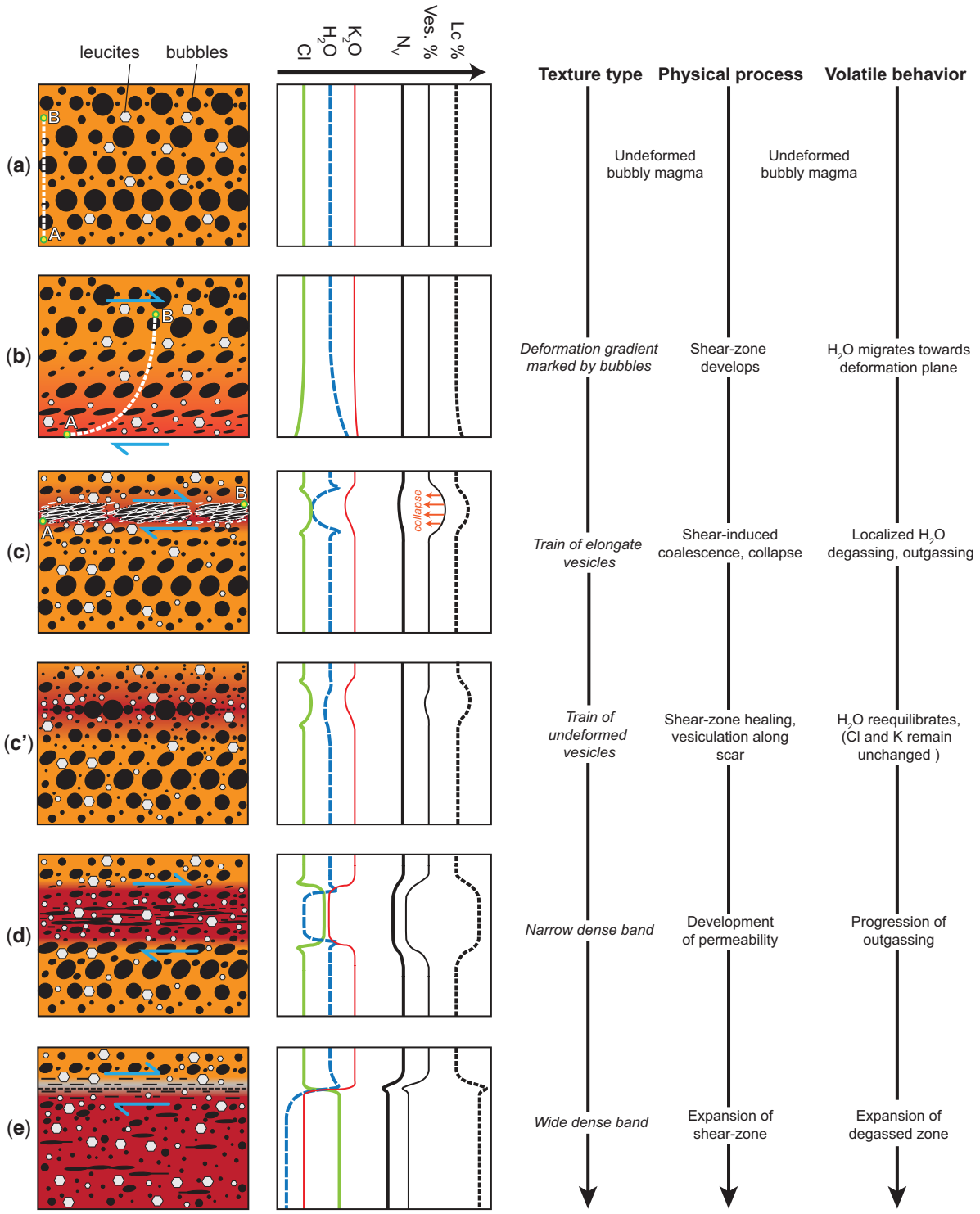

Fig. 14. Model for the formation of textural heterogeneities within pumice, modified from Shea *et al.* (2012). The left diagrams depict an ascending magma experiencing strain localization (direction of shear is parallel to ascent direction). Centre plots illustrate chemical (Cl, H_2O and K_2O) and textural (vesicle number density N_V, vesicularity and leucite fraction) variations that can be anticipated for each deformation step. Curves or lines represent hypothetical transects across the depicted models on the left. (a) Initial undeformed magma with homogeneous composition and texture. (b) Initiation of shearing; the bubbles and the melt deform and facilitate the migration of H_2O towards the zone of maximum strain. Leucite does not form but may mechanically accumulate within the strained zone. (c) The shear zone narrows as bubbles are forced into coalescence and trains of elongate vesicles become frequent. Within the zone of coalescence, bubbles become interconnected and H_2O is outgassed preferentially, inducing additional leucite crystallization and lowering of melt K_2O. In contrast, Cl is not degassed and stays within the melt. If this shear-zone becomes inactive (c'), the chemical gradients previously generated may either start to re-equilibrate (H_2O) or remain unchanged (K_2O, Cl) depending on the time available after shearing stops. If deformation continues (d), the zone of strain and shear-induced outgassing may widen and (e) form larger denser textural domains.

the melt may 'heal' and vesiculate further or deformed bubbles may relax back to spherical shapes (Fig. 14c'). In this case, partial re-equilibration of H_2O may occur.

(4) If strain localization is protracted at the same location, dense bands start to form and the H_2O-depleted, leucite-enriched zone widens (Fig. 14d). Such chemical zonations are exemplified by the maps shown in Fig. 11. By this time, shearing may also bring together portions of melt that have experienced slightly different evolutionary histories; for instance, the Na_2O–K_2O or Cl–H_2O compositional gaps in Fig. 8c argue in favor of two physically distinct magma regions that experienced different extents of degassing and leucite fractionation, which come together at some point during ascent.

(5) Eventually, dense shear bands become wide enough so that their boundaries are no longer visible at the clast scale (Fig. 8a). The wide, dense portions of the magma become relatively enriched in Cl following prolonged outgassing of H_2O and leucite crystallization (see Fig. 8b and c).

These preliminary results highlight the possible interpretative complications that arise even when high-quality analyses can be obtained. Heterogeneities within vesicular samples can effectively form at different stages of magma ascent and it is vital to recognize that not all will be associated with measurable chemical variations if some re-equilibration has occurred (e.g. 'dead' or inactive shear-zones). Thus, analyzing several species (i.e. fast and slow diffusers) is preferable when attempting to quantify potential re-equilibration timescales. Numerical models (Hale & Mühlhaus, 2007) and torsion experiments (Arbaret *et al.*, 2007; Okumura *et al.*, 2009; Laumonier *et al.*, 2011) also emphasize the importance of feedback processes associated with strain localization for magma rheology (Wright & Weinberg, 2009). Although the formation of shear-zones may provide degassing or outgassing pathways and reduce local pressure gradients and viscosity through slip surfaces, it can be expected that as shearing progresses, water is lost and crystallization is favored, thereby increasing magma viscosity and triggering complex rheological transitions (e.g. Arbaret *et al.*, 2007). Local increases in viscosity in turn should exacerbate the thickening of the shear-zones (i.e. free slip being efficient only at the shear-zone boundary), and eventually favor their delocalization or abandonment. Considering the ubiquity of textural features reminiscent of strain localization within the AD 79 pumice, the overall influence of shear-zones on magma rheology could be significant.

Clast-scale heterogeneities: implications for chemical analyses

There is mounting evidence that textural homogeneity of tephra clasts is more an exception than a rule. Although textural heterogeneity is obvious in certain samples (Martí *et al.*, 1999; Polacci *et al.*, 2001, 2003), the same cannot be said for all clasts. At Vesuvius, field sampling and initial visual inspection of pumices hardly reveals the true extent of their textural and chemical heterogeneity. Only through systematic sampling, preparation of thin sections, and detailed textural and chemical analyses do we begin to understand the first-order (i.e. large-scale) and second-order (i.e. small-scale) processes that generate them. The analysis of volatiles in vesicular samples, particularly H_2O, is still proving to be a technical challenge, and researchers frequently have to resort to bulk analyses and/or section their samples according to their textural domains (e.g. Balcone-Boissard *et al.*, 2008, 2011; Burgisser *et al.*, 2010; Neill *et al.*, 2010). Although such analyses can be more precise, they mask potential variations of ~1 wt % H_2O (see Fig. 8) or more. We also note that in our transect H_2O was more variable within vesicular regions of pumice clasts compared with dense regions (see standard deviations of H_2O concentrations in Fig. 8). This may reflect the presence of higher numbers of bubble–melt interfaces within vesicular zones that water can diffuse to, ultimately generating additional local volatile heterogeneities within the glass. Overall, this suggests that glasses analyzed in vesicular pyroclasts or zones in pyroclasts will generally be prone to larger H_2O variabilities compared with glasses analyzed in less vesicular regions.

The first set of systematic H_2O measurements presented here illustrates that (1) those variations are significant in frequency and amplitude even within a single clast, and that (2) microRaman analysis is a suitable and inexpensive tool to resolve even fine-scale degassing heterogeneities. New improved calibration routines for the analysis of H_2O in glasses using Raman spectroscopy are now available (Mercier *et al.*, 2010; Le Losq *et al.*, 2012) and their application to both experimental and natural samples will provide the research community with a new window into magma degassing processes.

CONCLUSIONS

The complexity and variability of vesicle and crystal textures within pumices generated during explosive eruptions warrants a careful examination of the small- and large-scale processes taking place during the course of magma ascent. Our study of Vesuvius AD 79 pumices illustrates how high spatial resolution analyses of pyroclast groundmass glass compositions and melt inclusions (volatiles and major elements) can reveal the various scales and the timing of degassing and crystallization. Whereas water is a 'fast diffuser' and provides an excellent record of the large-scale ascent history, chlorine is a 'slow diffuser' and can be used as a tracer of small-scale degassing processes. These two volatiles provide complementary information

that can potentially yield valuable constraints on (1) the timing of magma ascent, (2) the rates of degassing (i.e. at equilibrium or disequilibrium), and (3) the influence of conduit-wide and localized deformation on degassing and outgassing. Improving microanalytical techniques such as Raman analysis or EMPA to probe even the smallest spatial variations in H_2O (and possibly CO_2), S and the halogens will foster a much better understanding of the intricacies of magmatic volatile exsolution, which can be used to constrain petrological, physical and numerical models.

ACKNOWLEDGEMENTS

We are indebted to Editor Wendy Bohrson and reviewers Raffaello Cioni and Heather Wright, and an anonymous reviewer for their critical assessment of this work and the detailed comments, corrections and suggestions that improved the paper considerably. We thank Pavel Zinin, Jeff Taylor and Nicolas Cluzel, for their initial help with microRaman analysis. Jessica Larsen, Paul Wallace and Katie Kelley kindly provided glasses used for microRaman calibrations.

FUNDING

This work was supported by National Science Foundation (AR grants 1250366 and 8728) and H.T. was supported by the Royal Society University Research Fellowship.

SUPPLEMENTARY DATA

Supplementary data for this paper are available at *Journal of Petrology* online.

REFERENCES

Adams, N. K., Houghton, B. F. & Hildreth, W. (2006). Abrupt transitions during sustained explosive eruptions: examples from the 1912 eruption of Novarupta, Alaska. *Bulletin of Volcanology* **69**, 189–206.

Amalberti, J., Neuville, D. R., Sarda, P., Sator, N. & Guillot, B. (2011). *Mineralogical Magazine* **75**, 430 p.

Anovitz, L. M., Elam, J. M., Riciputi, L. R. & Cole, D. R. (1999). The failure of obsidian hydration dating: sources, implications and new directions. *Journal of Archaeological Science* **26**, 735–752.

Anovitz, L. M., Cole, D. R. & Fayek, M. (2008). Mechanisms of rhyolitic glass hydration below the glass transition. *American Mineralogist* **93**, 1166–1178.

Arbaret, L., Bystricky, M. & Champallier, R. (2007). Microstructures and rheology of hydrous synthetic magmatic suspensions deformed in torsion at high pressure. *Journal of Geophysical Research* **112**, B10208.

Baker, D. R. & Balcone-Boissard, H. (2009). Halogen diffusion in magmatic systems: Our current state of knowledge. *Chemical Geology* **263**, 82–88.

Balcone-Boissard, H., Villemant, B., Boudon, G. & Michel, A. (2008). Non volatile vs volatile behaviours of halogens during the AD 79 plinian eruption of Mt. Vesuvius, Italy. *Earth and Planetary Science Letters* **269**, 66–79, doi:10.1016/j.epsl.2008.02.003.

Balcone-Boissard, H., Villemant, B. & Boudon, G. (2010). Behaviour of halogens during the degassing of felsic magmas. *Geochemistry Geophysics Geosystems* **11**, Q09005, doi:10.1029/2010GC003028.

Balcone-Boissard, H., Boudon, G. & Villemant, B. (2011). Textural and geochemical constraints on eruptive style of the 79 AD eruption at Vesuvius. *Bulletin of Volcanology* **73**, 279–294.

Balcone-Boissard, H., Baker, D. R., Villemant, B. & Boudon, G. (2009). F and Cl diffusion in phonolitic melts: influence of the Na/K ratio. *Chemical Geology* **263**, 89–98.

Behrens, H., Roux, J., Neuville, D. R. & Siemann, M. (2006). Quantification of dissolved H_2O in silicate glasses using confocal microRaman spectroscopy. *Chemical Geology* **229**, 96–112.

Blundy, J. & Cashman, K. V. (2008). Petrological reconstruction of magmatic system variables and processes. In: Putirka, K. D. & Tepley, F. J., III (eds) *Minerals, Inclusions and Volcanic Processes. Mineralogical Society of America and Geochemical Society, Reviews in Mineralogy and Geochemistry* **69**, 179–239.

Burgisser, A. & Gardner, J. E. (2005). Experimental constraints on degassing and permeability in volcanic conduit flow. *Bulletin of Volcanology* **67**, 42–56.

Burgisser, A., Poussineau, S., Arbaret, L., Druitt, T. H., Giachetti, T. & Bourdier, J.-L. (2010). Pre-explosive conduit conditions of the 1997 Vulcanian explosions at Soufrière Hills Volcano, Montserrat: I. Pressure and vesicularity distributions. *Journal of Volcanology and Geothermal Research* **194**, 27–41.

Carroll, M. R. (2005). Chlorine solubility in evolved alkaline magmas. *Annals of Geophysics* **48**, 619–631.

Castro, J. M., Manga, M. & Martin, M. C. (2005). Vesiculation rates of obsidian domes inferred from H_2O concentration profiles. *Geophysical Research Letters* **32**, L21307.

Cimarelli, C., Di Traglia, F. & Taddeucci, J. (2010). Basaltic scoria textures from a zoned conduit as precursors to violent Strombolian activity. *Geology* **38**, 439–442.

Cioni, R. (2000). Volatile content and degassing processes in the 79AD magma chamber at Vesuvius (Italy). *Contributions to Mineralogy and Petrology* **140**, 40–54.

Cioni, R., Marianelli, P. & Sbrana, A. (1992). Dynamics of the AD 79 eruption: stratigraphic, sedimentological and geochemical data on the successions from the Somma–Vesuvius southern and eastern sectors. *Acta Vulcanologica* **2**, 109–123.

Cioni, R., Civetta, L., Marianelli, P., Metrich, N., Santacroce, R. & Sbrana, A. (1995). Compositional layering and syn-eruptive mixing of periodically refilled shallow magma chamber: the AD 79 Plinian eruption of Vesuvius. *Journal of Petrology* **36**, 739–776.

Cioni, R., Gurioli, L., Lanza, R. & Zanella, E. (2004). Temperatures of A.D. 79 pyroclastic density currents deposits (Vesuvius, Italy). *Journal of Geophysical Research* **109**, B02207.

Civetta, L., Galati, R. & Santacroce, R. (1991). Magma mixing and convective compositional layering within the Vesuvius magma chamber. *Bulletin of Volcanology* **53**, 287–300.

Degruyter, W., Bachmann, O. & Burgisser, A. (2010). Controls on magma permeability in the volcanic conduit during the climactic phase of the Kos Plateau Tuff eruption (Aegean Arc). *Bulletin of Volcanology* **72**, 63–74.

Denton, J. S., Tuffen, H. & Gilbert, J. S. (2012). Variations in hydration within perlitised rhyolitic lavas—evidence from Torfajökull, Iceland. *Journal of Volcanology and Geothermal Research* **223–224**, 64–73.

Denton, J. S., Tuffen, H., Gilbert, J. S. & Odling, N. (2009). The hydration and alteration of perlite and rhyolite. *Journal of the Geological Society* **166**, 895–904.

Devine, J. D., Gardner, J. E., Brack, H. P., Layne, G. D. & Rutherford, M. J. (1995). Comparison of microanalytical methods for estimating H_2O contents of silicic volcanic glasses. *American Mineralogist* **80**, 319–328.

Di Muro, A., Villemant, B., Montagnac, G., Scaillet, B. & Reynard, B. (2006). Quantification of water content and speciation in natural silicic glasses (phonolite, dacite, rhyolite) by confocal microRaman spectrometry. *Geochimica and Cosmochimica Acta* **70**, 2868–2884.

Friedman, I. & Smith, R. L. (1958). The deuterium content in some volcanic glasses. *Geochimica et Cosmochimica Acta* **15**, 218–228.

Frost, R. L., Martens, W. N. & Hales, M. C. (2009). Thermogravimetric analysis of selected group II carbonate minerals—implication for the geosequestration of greenhouse gases. *Journal of Thermal Analysis and Calorimetry* **95**, 999–1005.

Gardner, J. E., Burgisser, A., Hort, M. & Rutherford, M. J. (2006). Experimental and model constraints on degassing of magma during ascent and eruption. In: Siebe, C., Macias, J. L. & Aquirre-Diaz, G. J. (eds) *Neogene–Quaternary Continental Margin Volcanism: A Perspective from Mexico. Geological Society of America, Special Papers* **402**, 99–114.

Gardner, J. E., Befus, K. S., Watkins, J., Hesse, M. & Miller, N. (2012). Compositional gradients surrounding spherulites in obsidian and their relationship to spherulite growth and lava cooling. *Bulletin of Volcanology* **74**, 1865–1879.

Gertisser, R., Preece, K. & Keller, J. (2009). The Plinian Lower Pumice 2 eruption, Santorini, Greece: Magma evolution and volatile behavior. *Journal of Volcanology and Geothermal Research* **186**, 387–406.

Giachetti, T. & Gonnermann, H. M. (2013). Water in pumices: rehydration or incomplete degassing? *Earth and Planetary Science Letters* **369–370**, 317–332.

Giachetti, T., Druitt, T. H., Burgisser, A., Arbaret, L. & Galven, C. (2010). Bubble nucleation, growth and coalescence during the 1997 Vulcanian explosions of Soufrière Hills Volcano, Montserrat. *Journal of Volcanology and Geothermal Research* **193**, 215–231.

Gurioli, L., Cioni, R., Sbrana, A. & Zanella, E. (2002). Transport and deposition from pyroclastic flows over densely inhabited areas: Ercolano, Italy. *Sedimentology* **46**, 1–26.

Gurioli, L., Houghton, B. F., Cashman, K. V. & Cioni, R. (2005). Complex changes in eruption dynamics during the AD 79 eruption of Vesuvius. *Bulletin of Volcanology* **67**, 144–159.

Hale, A. J. & Mühlhaus, H.-B. (2007). Modelling shear bands in a volcanic conduit: Implications for over-pressures and extrusion rates. *Earth and Planetary Science Letters* **263**, 74–87.

Hauri, E., Wang, J., Dixen, J. E., King, P. L., Mandeville, C. & Newman, S. (2002). SIMS analysis of volatiles in silicate glasses. 1. Calibration, matrix effects and comparisons with FTIR. *Chemical Geology* **183**, 99–114.

Hess, K.-U., Cordonnier, B., Lavallee, Y. & Dingwell, D. B. (2008). Viscous heating in rhyolite: An *in-situ* experimental determination. *Earth and Planetary Science Letters* **275**, 121–126.

Houghton, B. F. & Wilson, C. J. N. (1989). A vesicularity index for pyroclast deposits. *Bulletin of Volcanology* **51**, 451–462.

Iacono-Marziano, G., Schmidt, B. C. & Dolfi, D. (2007). Equilibrium and diseqilibrium degassing of a phonolitic melt (Vesuvius AD 79 'white pumice') simulated by decompression experiments. *Journal of Volcanology and Geothermal Research* **161**, 151–164.

Ihinger, P. D., Hervig, R. L. & McMillan, P. F. (1994). Analytical methods for volatiles in glasses. In: Carroll, M. R. & Holloway, J. R. (eds) *Volatiles in Magmas. Mineralogical Society of America, Reviews in Mineralogy* **30**, 67–121.

Jarosewich, E., Nelen, J. A. & Norberg, J. A. (1980). Reference samples for electron microprobe analysis. *Geostandards Newsletter* **4**, 43–47.

Kelley, K. A. & Cottrell, E. (2012). The influence of magmatic differentiation on the oxidation state of Fe in a basaltic arc magma. *Earth and Planetary Science Letters* **329–330**, 109–121.

Kent, A. J. R. (2008). Melt inclusions in basaltic and related volcanic rocks. In: Putirka, K. D. & Tepley, F. J., III (eds) *Minerals, Inclusions and Volcanic Processes. Mineralogical Society of America and Geochemical Society, Reviews in Mineralogy and Geochemistry* **69**, 273–332.

Larsen, J. F. (2008). Heterogeneous bubble nucleation and disequilibrium H_2O exsolution in Vesuvius K-phonolite melts. *Journal of Volcanology and Geothermal Research* **175**, 278–288.

Laumonier, M., Arbaret, L., Burgisser, A. & Champallier, R. (2011). Porosity redistribution enhanced by strain localization in crystal-rich magmas. *Geology* **39**, 715–718.

Lautze, N. & Houghton, B. F. (2007). Linking explosion intensity and magma rheology during 2002 at Stromboli volcano. *Bulletin of Volcanology* **69**, 445–460.

Le Losq, C., Neuville, D. R., Moretti, R. & Roux, J. (2012). Determination of water content in silicate glasses using Raman spectrometry: Implications for the study of explosive volcanism. *American Mineralogist* **97**, 779–790.

Lesne, P., Kohn, S. C., Blundy, J., Witham, F., Botcharnikov, R. E. & Behrens, H. (2011). Experimental simulation of closed-system degassing in the system basalt–H_2O–CO_2–S–Cl. *Journal of Petrology* **52**, 1737–1762.

Llewellin, E. W., Mader, H. M. & Wilson, S. D. R. (2002). The rheology of a bubbly liquid. *Proceedings of the Royal Society of London, Series A* **458**, 987–1016.

Lowenstern, J. B. (2000). A review of the contrasting behavior of two magmatic volatiles: chlorine and carbon dioxide. *Journal of Geochemical Exploration* **69–70**, 287–290.

Lyakhovsky, V., Hurwitz, S. & Navon, O. (1996). Bubble growth in rhyolitic melts: Experimental and numerical investigation. *Bulletin of Volcanology* **58**, 19–32.

Martí, J., Soriano, C. & Dingwell, D. B. (1999). Tube pumices as strain markers of the ductile–brittle transition during magma fragmentation. *Nature* **402**, 650–653.

McMillan, P. (1984). Structural studies of silicate glasses and melts—applications and limitations of Raman spectroscopy. *American Mineralogist* **69**, 622–644.

Mercier, M., Di Muro, A., Giordano, D., Metrich, N., Lesne, P., Pichavant, M., Scaillet, B., Clocchiatti, R. & Montagnac, G. (2009). Influence of glass polymerisation and oxidation on micro-Raman water analysis in alumino-silicate glasses. *Geochim. Cosmochim. Acta* **73**, 197–217.

Mercier, M., Di Muro, A., Metrich, N., Giordano, D., Belhadj, O. & Mandeville, C. W. (2010). Spectroscopic analysis (FTIR, Raman) of water in mafic and intermediate glasses and glass inclusions. *Geochimica et Cosmochimica Acta* **74**, 5641–5656.

Métrich, N. & Wallace, P. J. (2008). Volatile abundances in basaltic magmas and their degassing paths tracked by melt inclusions. In: Putirka, K. D. & Tepley, F. J., III (eds) *Minerals, Inclusions and Volcanic Processes. Mineralogical Society of America and Geochemical Society, Reviews in Mineralogy and Geochemistry* **69**, 363–402.

Métrich, N., Bertagnini, A. & Di Muro, A. (2010). Conditions of Magma Storage, Degassing and Ascent at Stromboli: New Insights into the Volcano Plumbing System with Inference on the Eruptive Dynamics. *Journal of Petrology* **51**, 603–626.

Michaud, V., Clocchiatti, R. & Sbrana, S. (2000). The Minoan and post-Minoan eruptions, Santorini (Greece), in the light of melt inclusions: chlorine and sulphur behavior. *Journal of Volcanology and Geothermal Research* **99**, 195–214.

Morgan, D. J., Blake, S., Rogers, N. W., De Vivo, B., Rolandi, G. & Davidson, J. P. (2006). Magma chamber recharge at Vesuvius in the century prior to the eruption of A.D. 79. *Geology* **34**, 845–848.

Morizet, Y., Brooker, R. A., Iacono-Marziano, G. & Kjarsgaard, B. A. (2013). Quantification of dissolved CO2 in silicate glasses using Micro-Raman spectroscopy. *American Mineralogist* **98**, 1788–1802.

Mues-Schumacher, U. (1994). Chemical variations of the A.D. 79 pumice deposits of Vesuvius. *European Journal of Mineralogy* **6**, 387–395.

Mysen, B. & Richet, P. (2005). *Silicate Glasses and Melts: Properties and Structure.* Elsevier, 544 p.

Neill, O. K., Hammer, J. E., Izbekov, P., Belousova, M. G., Belousov, A. B., Clarke, A. B. & Voight, B. (2010). Influence of pre-eruptive degassing and crystallization on the juvenile products of laterally directed volcanic explosions. *Journal of Volcanology and Geothermal Research* **198**, 264–274.

Neuhoff, P. S. & Wang, J. (2007). Isothermal measurement of heats of hydration in zeolites by simultaneous thermogravimetry and differential scanning calorimetry. *Clays and Clay Minerals* **55**, 239–252.

Okumura, S., Nakamura, S., Takeuchi, S., Tsuchiyama, A., Nakano, T. & Uesugi, K. (2009). Magma deformation may induce non-explosive volcanism via degassing through bubble networks. *Earth and Planetary Science Letters* **281**, 267–274.

Polacci, M., Papale, P. & Rosi, M. (2001). Textural heterogeneities in pumices from the climactic eruption of Mt. Pinatubo, 15 June 1991, and implications for magma ascent dynamics. *Bulletin of Volcanology* **63**, 83–97.

Polacci, M., Pioli, L. & Rosi, M. (2003). The Plinian phase of the Campanian Ignimbrite eruption (Phlegraean Fields, Italy): evidence from density measurements and textural characterization of pumice. *Bulletin of Volcanology* **65**, 418–432.

Putnis, C. V., Geisler, T., Schmid-Beurmann, P., Stephan, T. & Giampaolo, C. (2007). An experimental study of the replacement of leucite by analcime. *American Mineralogist* **92**, 19–26.

Roulia, M., Chassapis, K., Kapoutsis, J. A., Kamitsos, E. I. & Savvidis, T. (2006). Influence of thermal treatment on the water release and the glassy structure of perlite. *Journal of Material Science* **41**, 5870–5881.

Rosi, M., Landi, P., Polacci, M., Di Muro, A. & Zandomeneghi, D. (2004). Role of conduit shear on ascent of the crystal-rich magma feeding the 800-year-B.P. Plinian eruption of Quilotoa volcano (Ecuador). *Bulletin of Volcanology* **66**, 307–321.

Rutherford, M. J. (2008). Magma ascent rates. *Reviews in Mineralogy and Geochemistry* **69**, 241–271.

Scaillet, B., Pichavant, M. & Cioni, R. (2008). Upward migration of Vesuvius magma chamber over the past 20,000 years. *Nature* **455**, 216–219.

Shea, T., Larsen, J. F., Gurioli, L., Hammer, J. E., Houghton, B. F. & Cioni, R. (2009). Leucite crystals: surviving witnesses of magmatic processes preceding the AD79 eruption at Vesuvius, Italy. *Earth and Planetary Science Letters* **281**, 88–98.

Shea, T., Gurioli, L., Larsen, J., Houghton, B. F., Hammer, J. E. & Cashman, K. V. (2010*a*). Linking experimental and natural vesicle textures in Vesuvius AD79 white pumice. *Journal of Volcanology and Geothermal Research* **192**, 69–84.

Shea, T., Houghton, B. F., Gurioli, L., Cashman, K. V., Hammer, J. E. & Hobden, B. V. (2010*b*). Textural analyses of vesicles in volcanic rocks: an integrated methodology. *Journal of Volcanology and Geothermal Research* **190**, 271–289.

Shea, T., Gurioli, L., Houghton, B. F., Cioni, R. & Cashman, K. V. (2011). Column collapse and generation of pyroclastic density currents during the A.D. 79 eruption of Vesuvius: The role of pyroclast density. *Geology* **39**, 695–698.

Shea, T., Gurioli, L. & Houghton, B. F. (2012). Transitions between fall phases and pyroclastic density currents during the AD 79 eruption at Vesuvius: building a transient conduit model from the textural and volatile record. *Bulletin of Volcanology* **74**, 2363–2381.

Signorelli, S. & Capaccioni, B. (1999). Behaviour of chlorine prior and during the 79 A.D. plinian eruption of Vesuvius (southern Italy) as inferred from the present distribution in glassy mesostase and whole-pumices. *Lithos* **46**, 715–730.

Signorelli, S. & Carroll, M. R. (2000). Solubility and fluid–melt partitioning of Cl in hydrous phonolitic melts. *Geochimica et Cosmochimica Acta* **64**, 2851–2862.

Sigurdsson, H., Carey, S., Cornell, W. & Pescatore, T. (1985). The eruption of Vesuvius in A.D. 79. *National Geographic Research* **1**, 332–387.

Sigurdsson, H., Cornell, W. & Carey, S. (1990). Influence of magma withdrawal on compositional gradients during the AD 79 Vesuvius eruption. *Nature* **345**, 519–521.

Sparks, R. S. J., Barclay, J., Jaupart, C., Mader, H. M. & Phillips, J. C. (1994). Physical aspects of magmatic degassing I. Experimental and theoretical constraints on vesiculation. In: Carroll, M. R. & Holloway, J. R. (eds) *Volatiles in Magmas. Mineralogical Society of America, Reviews in Mineralogy* **30**, 413–445.

Stasiuk, M. V., Barclay, J., Carroll, M. R., Jaupart, C., Ratte, J. C., Sparks, R. S. J. & Tait, S. R. (1996). Degassing during magma ascent in the Mule Creek vent (USA). *Bulletin of Volcanology* **58**, 117–130.

Thomas, R. (2000). Determination of water contents of granite melt inclusions by confocal laser Raman microprobe spectroscopy. *American Mineralogist* **85**, 868–872.

Tuffen, H., Dingwell, D. B. & Pinkerton, H. (2003). Repeated fracture and healing of silicic magma generate flow banding and earthquakes? *Geology* **31**, 1089–1092.

Tuffen, H., Owen, J. & Denton, J. S. (2010). Magma degassing during subglacial eruptions and its use to reconstruct palaeo-ice thicknesses. *Earth-Science Reviews* **99**, 1–18.

Tuffen, H., Owen, J. & Applegarth, L. J. (2012). Measurement of volatile concentrations in volcanic glasses using thermogravimetric analysis: comparison with micro-analytical methods. *Geophysical Research Abstracts* **14**, EGU2012–11347.

Watson, E. B. (1994). Diffusion in volatile-bearing magmas. In: Carroll, M. R. & Holloway, J. R. (eds) *Volatiles in Magmas. Mineralogical Society of America, Reviews in Mineralogy* **30**, , 371–411.

Webster, J. D. (2004). The exsolution of magmatic hydrosaline chlorine liquids. *Chemical Geology* **210**, 33–48.

Wright, H. M. N. & Weinberg, R. F. (2009). Strain localization in vesicular magmas: Implications for rheology and fragmentation. *Geology* **37**, 1023–1026.

Wright, H. M. N., Folkes, C. B., Cas, R. A. F. & Cashman, K. V. (2011). Heterogeneous pumice populations in the 2·08-Ma Cerro Galan Ignimbrite: implications for magma recharge and ascent preceding a large-volume silicic eruption. *Bulletin of Volcanology* **73**, 1513–1533.

Zajacz, Z., Halter, W., Malfait, W. J., Bachmann, O., Bodnar, R. J., Hirschmann, M. M., Mandeville, C. W., Morizet, Y., Muntener, O., Ulmer, P. & Webster, J. D. (2005). A composition-independent quantitative determination of the water content in silicate glasses and silicate melt inclusions by confocal Raman spectrometry. *Contributions to Mineralogy and Petrology* **150**, 631–642.

Yokohama, T., Okumura, T. & Nakashima, S. (2008). Hydration of rhyolitic glass during weathering as characterized by IR microspectroscopy. *Geochimica et Cosmochimica Acta* **72**, 117–125.

Zellmer, G. F. & Clavero, J. E. (2006). Using trace element correlation patterns to decipher a sanidine crystal growth chronology: an example from Taapaca volcano, Central Andes. *Journal of Volcanology and Geothermal Research* **156**, 291–301.